A width-averaged hydrodynamic model of two-layer tidal circulation

by

A.F. Schiereck

to obtain the degree of Bachelor of Science
at the Delft University of Technology.

Student number:	4389050	
Project duration:	September 16, 2019 – January 29, 2020	
Thesis committee:	Dr. H. M. Schuttelaars,	TU Delft, supervisor
	Dr. S. R. de Roode,	TU Delft, supervisor
	Dr. ir. L. J. J. van Iersel,	TU Delft
	Dr. ir. M. Rohde,	TU Delft

TU Delft

Abstract

Estuaries support a unique hydrodynamic system due to the fresh water flowing into a salt water sea. This leads to stratification which can significantly alter internal tidal dynamics in the estuary. A model has been developed by Winant (2010) to describe the water motions of a two-layer system in tidal basin. The aim of this thesis is provide an extension to this model by parameterizing bottom stress using a partial slip parameter and viscosity. Also level variations of the bed are taken into account in this thesis. A width-averaged model of an idealized stratified tidal basin is developed. With increased bottom stress, the velocity near the bed is significantly slowed down, whereas increasing the viscosity slows down the velocity further away from the bed. The interface fluctuates more when the viscosity is low, the wavelength of these fluctuations is decreased with increasing viscosity. Resonance characteristics in the hydrodynamics are dampened severely by increased viscosity, and less by bottom stress. Increasing the slope of the bed results in a lag of tidal dynamics at the end of the embayment compared to at the embayment entrance. A sloped bed also dampens the resonance characteristics.

Contents

1

Introduction

The water in the oceans and seas on earth is in constantly motion. As a result of the gravitational forces of the moon and sun, sea levels rise and fall in a perpetual motion. According to Gerkema (2019), in most places high and low water each occur about twice a day, forming the semi-diurnal tide. The gravitational pull of the moon that causes the semi-diurnal tide is depicted in figure 1.1. The part of the earth that is closest to the moon experiences high tide because of gravitational forces from the moon, while the opposite side experiences high tide because of centrifugal forces. In between water is pulled away by both these forces and low tide occurs. As the earth rotates around its axis each day, each geographical location experiences high and low tide twice a day.

While the difference in surface elevation between high and low tide at the ocean is generally around half a meter , the tidal range can be much larger in embayments that are predominantly surrounded by coastlines but are connected to an ocean or sea. Here, if the circumstances are right, the incoming tide can drive up the water level to much greater heights. This is the case in the Bay of Fundy in Canada, for example, where the tidal range is 13 meters. In figure 1.2, a photograph of the Hopewell rocks in the Bay of Fundy at low tide is shown.

Figure 1.1: A schematic illustration of earth-moon tide system. Illustration by time and date

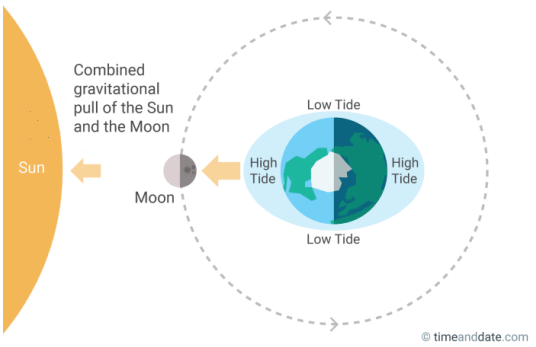

Figure 1.2: Low tide at the Hopewell rocks, Bay of Fundy. Photo by Bay of Fundy Tourism

The field of coastal hydrodynamics seeks to understand and predict the behavior of the tides in bays, estuaries and other coastal bodies of water. Estuaries are defined by Cameron and Pritchard (1963) as: a semi-enclosed coastal body of water, which has a free connection with the open sea, and within which seawater is measurably diluted with freshwater derived from land drainage. Estuaries form a unique habitat for various animal and plant species, and can function as a navigational route between the ocean and inland territories. It is important to know how the hydrodynamics in estuaries are changed due to human activities such as dredging or building dams. The water in estuaries can be stratified, the fresh water from the river, which

Figure 1.3: A schematic illustration of the partial slip condition. The arrows indicate the velocity profile. On the left a no slip condition at the bottom is illustrated. The velocity profiles on the left do not extend all the way to the bottom, but end at the top of the boundary layer. Here the flow velocity is related to the vertical rate-of-change of the velocity, by the partial slip parameter λ. When $\lambda = 0$, the flow is not slowed down near the bottom. With increasing λ, the flow is increasingly slowed down near the bottom.

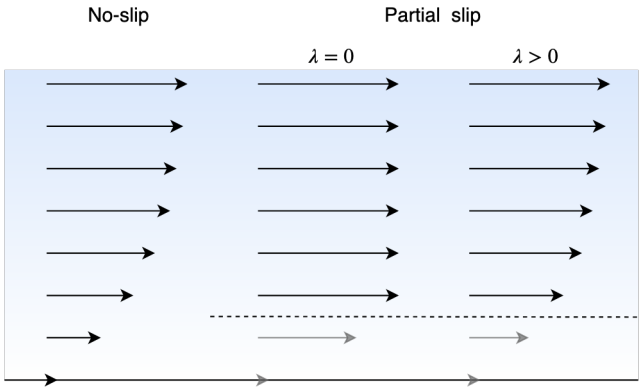

has a slightly lower density, and the salt water from the ocean, which has a slightly higher density, form two separate layers. This stratification can have significant effects on the hydrodynamics in the basin. In this thesis, the internal dynamics of idealized stratified tidal embayments are studied. The aim of this study is to develop and analyze a model that is an extension on existing research by generalizing some assumptions.

Winant (2010) developed a three-dimensional model for an idealized stratified tidal basin, to investigate the influence of external tidal forcing at the surface on the internal dynamics of a two-layer system. The two-layer system not only supports tidal waves that are similar to the tidal waves in a one-layer system, but also gives rise to interfacial tides. The Upper Loch Linnhe is an example where these interfacial tides are significant, as currents are observed that are 10 times larger than expected based on a one-layer model. The model developed by Winant assumes the basin has a constant depth. The bottom friction is described by a no-slip condition, i.e. the flow velocity at the bed of the basin is prescribed to be zero. Internal friction caused by turbulent flow is parameterized by eddy viscosities. Stresses that arise from this turbulence are taken to be proportional to the flow-velocity gradient. The proportionality parameters are taken to be constant and are called eddy viscosity coefficients.
As long as friction is not dominant, near-standing waves are present in both the free water surface as the interface between the two layers of water. Wave patterns on the interface are characterized by smaller wavelengths than the free surface. If the embayment-length is near resonance, flow velocities and tidal ranges for both the free surface and the interface are amplified. The internal tidal dynamics of the embayment are sensitive to the density anomaly, as a result the behavior of the free surface and interface vary intensely as a result of small changes in the density.

Chernetsky (2012) and Dijkstra et al. (2017) have formulated width-averaged models for an idealized tidal basin. These models assume constant water density everywhere, so a stratified two-layer system cannot be described by these models. These models do include the effects of a variable bed. Internal friction due to turbulent flow is parameterized by constant eddy viscosity coefficients, in a similar manner as in Winant (2010). The bottom friction is described using a partial slip parameter. When a partial slip condition is imposed, the domain on which the model is solved doesn't extend all the way to the bed of the embayment, but instead ends at the top of the boundary layer. Here the flow velocity is related to the rate-of-change in the vertical direction of the horizontal flow velocity by the so-called partial slip parameter. This parameter can be varied to model different types of bottom stress. In figure 1.3 a schematic illustration of the partial slip condition is given. If the horizontal velocity in figure 1.3 is denoted by u, and z is the vertical direction, then the partial slip condition reads $\frac{\partial u}{\partial z} = \lambda u$. Here λ is the partial slip parameter.
Since these models do not extend to the bottom but end at the top of the boundary condition, the eddy viscosity is only assumed to be constant above the boundary layer. There are no restrictions on the eddy viscosity in the boundary layer.

The aim of this thesis is to develop a model that is an extension on the model developed by Winant (2010), by allowing level variations of the bed and imposing a partial slip condition instead of a no-slip condition so that the bottom stress can be varied.

This model is developed by applying the methods used by Chernetsky (2012) and Dijkstra et al. (2017) to a two-layer system.

The results from this model are compared to the results from Winant (2010) to answer the two main research questions of this thesis:

1. How does bottom stress affect the internal tides in a stratified tidal basin?
2. How does a variable bed affect the internal tides in a stratified tidal basin?

In order to answer these questions, a model will be formulated in chapter 2, starting from the conservation laws of fluid dynamics. The law of conservation of mass and the law of conservation of momentum are width-averaged and combined with the appropriate boundary conditions. The obtained balances undergo a scaling analysis, where the relative importance of different terms in each equation is determined. The leading order system is set up, which consists of only the most important terms of each equation and the boundary conditions. This leading order system is solved using a numerical second-order finite difference method. The results from this model are presented in chapter 3. In chapter 4 these results are analyzed and the research questions are answered.

2

Model derivation

In this chapter a width-averaged model of the tidal dynamics in an idealized stratified basin is derived from the physical laws for conservation of mass and momentum.
In the first section the geometry of the two-layer basin is outlined. Next the width-averaged continuity equation is derived from the three-dimensional law of conservation of mass and subsequently the width-averaged momentum equation from the law of conservation of momentum. Subsequently the boundary conditions are discussed. Lastly, the resulting equations and boundary conditions are scaled to derive the leading-order equations.

2.1. Geometry

An overview of the geometry of the embayment is depicted in figure 2.1.

Figure 2.1: A top view and a side view of the geometry of the embayment.

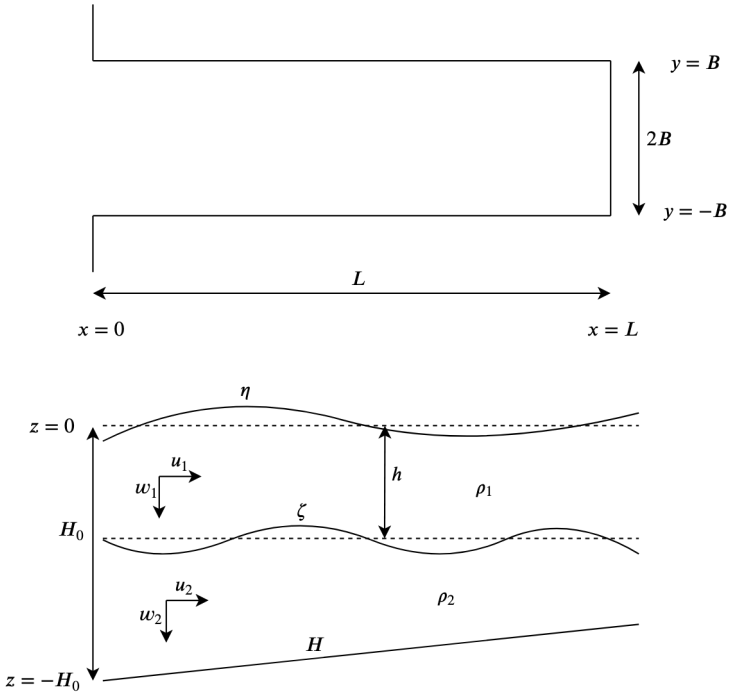

The embayment is taken to be rectangular, having a constant width B and length L. The water depth at the seaward boundary of the channel is H_0, where $H_0 \ll L$. The water depth in the interior of the channel is given by $H^*(x, y)$. The coordinate system is chosen such that $x = 0$ is found at the seaward boundary and $x = L$ at the coastal boundary, $z = 0$ at the undisturbed water surface and $z = -H^*$ denotes the location of the

bottom, and the side walls of the channel are found at $y = \pm B$. The free surface is described by $\eta^*(x, y, t)$.
The basin is assumed to be stratified, and two layers of water of different density can be identified in the embayment. The undisturbed interface of the two layers is located at $z = -h$, where the interface-depth h is assumed to be constant. Variations of the interface are denoted by $\zeta^*(x, y, t)$, therefore the interface is located at $z = -h + \zeta^*$. All variables and constants concerning one of the layers are denoted with a subscript 1 for the top layer and a subscript 2 for the bottom layer.
The density ρ is assumed to be constant within each layer:

$$\rho = \begin{cases} \rho_1 & \zeta^* < z < \eta^*, \\ \rho_2 & -H^* < z < \zeta^*, \end{cases} \tag{2.1}$$

The velocity vector is given by $\vec{u_i}^*(x, y, z, t) = (u_i^*, v_i^*, w_i^*)$ in layer i, with $i \in \{1, 2\}$. Here u_i^*, v_i^* and w_i^* are the velocity-components in the x-, y- and z-direction, respectively.
The width-averaged velocity in the x-direction is defined as

$$u(x, z, t) = \frac{1}{2B} \int_{-B}^{B} u^* \, \mathrm{d}y. \tag{2.2}$$

with similar expressions for the width averaged velocity in the z-direction, the width averaged water-depth, the width averaged free surface and the width averaged interface.

2.2. Continuity equation

In this section the width-integrated continuity equation is derived from the three-dimensional law of conservation of mass. Since the water in the embayment consists of two separate layers, therefore the law of conservation of mass is applied to each layer separately. These layers will be indicated by the subscript i, with $i \in \{1, 2\}$.
The law of conservation of mass for each layer is given by

$$\frac{\partial \rho_i}{\partial t} + \nabla \cdot (\rho_i \vec{u_i}^*) = 0.$$

By assuming the density within each layer to be constant, both its time- and space-derivative drop out. Rewriting yields the three-dimensional continuity equation for incompressible flow:

$$\frac{\partial u_i^*}{\partial x} + \frac{\partial v_i^*}{\partial y} + \frac{\partial w_i^*}{\partial z} = 0. \tag{2.3}$$

Averaging the three-dimensional continuity equation over the width of the channel yields

$$\frac{1}{2B} \left(\int_{-B}^{B} \frac{\partial u_i^*}{\partial x} \mathrm{d}y + \left[v_i^* \right]_{-B}^{B} + \int_{-B}^{B} \frac{\partial w_i^*}{\partial z} \mathrm{d}y \right) = 0.$$

Now the Leibnitz integral rule for integrals with constant boundaries is used to switch the order of integration and differentiation. Also the definitions for the width-averaged velocities, given by Eq. (2.2), are applied. Next the condition that the side walls are impermeable, i.e. $v^* = 0$ at $y = \pm B$, is employed to eliminate $\left[v_i^* \right]_{-B}^{B}$. This finally results in the width-averaged continuity equations

$$\frac{\partial u_i}{\partial x} + \frac{\partial w_i}{\partial z} = 0. \tag{2.4}$$

2.3. Momentum equation

In this section the width-averaged momentum equation is derived from the law of conservation of momentum. Neglecting Coriolis effects, this law is given by

$$\rho \frac{D\vec{u}^*}{Dt} = -\vec{\nabla} p + \vec{\nabla} \tau + \rho \vec{g}.$$

Here $\vec{\nabla} = \left(\frac{\partial}{\partial x}, \frac{\partial}{\partial y}, \frac{\partial}{\partial z}\right)$ is the nabla operator, p is the pressure and $\vec{g}$ is the gravitational acceleration. The turbulent Reynolds stress tensor is denoted by τ and is given by

$$\tau = \begin{bmatrix} \tau_{xx} & \tau_{xy} & \tau_{xz} \\ \tau_{yx} & \tau_{yy} & \tau_{yz} \\ \tau_{zx} & \tau_{zy} & \tau_{zz} \end{bmatrix}.$$

In this tensor, for example, τ_{xy} represents the x-component of the turbulent shear stress that acts on on a surface normal to the y-direction. As discussed in Pedlosky (1987) Pedlosky (1987), these stresses refer to small length and time scale turbulent flow compared to the length and time scale of the total averaged flow. All other terms in the momentum equation refer to averaged, large scale flow.
The total derivative $\frac{D\vec{u}^*}{Dt}$ is given by

$$\frac{D\vec{u}^*}{Dt} = \frac{\partial \vec{u}^*}{\partial t} + \vec{u}^* \cdot \vec{\nabla}\vec{u}^* = \begin{bmatrix} \frac{\partial u^*}{\partial t} + u^* \frac{\partial u^*}{\partial x} + v^* \frac{\partial u^*}{\partial y} + w^* \frac{\partial u^*}{\partial z} \\ \frac{\partial v^*}{\partial t} + u^* \frac{\partial v^*}{\partial x} + v^* \frac{\partial v^*}{\partial y} + w^* \frac{\partial v^*}{\partial z} \\ \frac{\partial w^*}{\partial t} + u^* \frac{\partial w^*}{\partial x} + v^* \frac{\partial w^*}{\partial y} + w^* \frac{\partial w^*}{\partial z} \end{bmatrix}.$$

2.3.1. The vertical balance

Because the embayment is assumed to be shallow, scaling arguments can be used to show that the vertical component of this momentum balance reduces to the hydrostatic balance Pedlosky (1987)

$$\frac{\partial p}{\partial z} = -\rho \vec{g} \Rightarrow p = \vec{g} \int_z^{\eta^*} \rho(z') \mathrm{d}z' + p_a,$$

where the pressure at the free surface must be equal to the atmopheric pressure: $p\big|_{z=\eta} = p_a$. Using the expression for the density (Eq. (2.1)) yields:

$$p = \begin{cases} p_1 = -g\rho_1(z-\eta^*) + p_a & \zeta^* < z < \eta^*, \\ p_2 = -g\rho_2(z-\zeta^*) - g\rho_1(\zeta^* - \eta^*) + p_a & -H^* < z < \zeta^*. \end{cases} \tag{2.5}$$

2.3.2. The horizontal balance

The horizontal component of the momentum balance in the $x-$direction is given by

$$\rho_i \left(\frac{\partial u_i^*}{\partial t} + u_i^* \frac{\partial u_i^*}{\partial x} + v_i^* \frac{\partial u_i^*}{\partial y} + w_i^* \frac{\partial u_i^*}{\partial z} \right) = -\frac{\partial p_i}{\partial x} + \left(\frac{\partial \tau_{xx}}{\partial x} + \frac{\partial \tau_{xy}}{\partial y} + \frac{\partial \tau_{xz}}{\partial z} \right). \tag{2.6}$$

A closure relation is needed to relate the turbulent Reynolds stesses to state variables. The following simple and often used closure scheme is proposed by Pedlosky (1987, p.183) Pedlosky (1987)

$$\tau_{xx} = 2\rho_i \tilde{A_h} \frac{\partial u_i^*}{\partial x}, \qquad \tau_{xy} = \rho_i \tilde{A_h} \left(\frac{\partial u_i^*}{\partial y} + \frac{\partial v_i^*}{\partial x} \right), \qquad \tau_{xz} = \rho_i \left(\tilde{A_v} \frac{\partial u_i^*}{\partial z} + \tilde{A_h} \frac{\partial w_i^*}{\partial x} \right),$$

with $\tilde{A_h}$ and $\tilde{A_v}$ the horizontal and vertical eddy viscosity coefficients. These eddy viscosities represent the effects of processes with small length and time scales relative to the explicitly resolved phenomena, i.e. $\vec{u}^*$, η^* and ζ^*. In the following, these coefficients are assumed to be constant.
Since the derivation of the bottom layer is similar to that of the top layer, the derivation will only be outlined for the top water layer, above the interface, i.e. $z > \zeta^*$.
As a first step the expression for pressure as given by Eq. (2.5) is differentiated with respect to x, so that it can be substituted in the horizontal component of the momentum balance (Eq.(2.6)). For the top layer, this yields

$$\frac{\partial p_1}{\partial x} = -g\rho_1 \frac{\partial \eta^*}{\partial x}, \tag{2.7}$$

spatial variations in the atmospheric pressure $\left(\frac{\partial p_a}{\partial x}\right)$ are neglected.

Next, the right hand side of the horizontal component of the momentum-balance for the top layer (Eq. 2.6 with $i = 1$) is combined with the pressure-dervative as given by Eq. (2.7) and the closure scheme and divided

by ρ_1. This gives

$$-g\frac{\partial \eta^*}{\partial x}+\frac{\partial}{\partial x}\left(2\tilde{A}_h\frac{\partial u_1^*}{\partial x}\right)+\frac{\partial}{\partial y}\left(\tilde{A}_h\frac{\partial u_1^*}{\partial y}+\tilde{A}_h\frac{\partial v_1^*}{\partial x}\right)+\frac{\partial}{\partial z}\left(\tilde{A}_v\frac{\partial u_1^*}{\partial z}+\tilde{A}_h\frac{\partial w_1^*}{\partial x}\right).$$

The three-dimensional continuity equation can be used to cancel out some terms, resulting in

$$-g\frac{\partial \eta^*}{\partial x}+\frac{\partial}{\partial x}\left(\tilde{A}_h\frac{\partial u_1^*}{\partial x}\right)+\frac{\partial}{\partial y}\left(\tilde{A}_h\frac{\partial u_1^*}{\partial y}\right)+\frac{\partial}{\partial z}\left(\tilde{A}_v\frac{\partial u_1^*}{\partial z}\right).$$

Now this expression is averaged over the width using the Leibnitz integral rule for integrals with constant boundaries. This following expression is obtained:

$$\frac{1}{2B}\left(-g\frac{\partial}{\partial x}\int_{-B}^{B}\eta^*\,\mathrm{d}y+\frac{\partial}{\partial x}\left(\tilde{A}_h\frac{\partial}{\partial x}\int_{-B}^{B}u_1^*\,\mathrm{d}y\right)+\left[\tilde{A}_h\frac{\partial u_1^*}{\partial y}\right]_{-B}^{B}+\frac{\partial}{\partial z}\left(\tilde{A}_v\frac{\partial}{\partial z}\int_{-B}^{B}u_1^*\,\mathrm{d}y\right)\right).$$

Assuming the side walls are stress-free, i.e. $\tilde{A}_h\frac{\partial u^*}{\partial y}=0$ at $y=\pm B$ and using the width-averaged variables u_1 and η yields the final expression for the right hand side:

$$-g\frac{\partial \eta}{\partial x}+\frac{\partial}{\partial x}\left(\tilde{A}_h\frac{\partial u_1}{\partial x}\right)+\frac{\partial}{\partial z}\left(\tilde{A}_v\frac{\partial u_1}{\partial z}\right).$$

As a final step the left hand side of the momentum balance for the top layer (Eq. (2.6) with $i=1$) is divided by ρ_1 and the three-dimensional continuity equation (Eq. (2.3)), multiplied by u_1^*, is added to the left-hand side of this equation, resulting in

$$\frac{\partial u_1^*}{\partial t}+u_1^*\frac{\partial u_1^*}{\partial x}+u_1^*\frac{\partial u_1^*}{\partial x}+v_1^*\frac{\partial u_1^*}{\partial y}+u_1^*\frac{\partial v_1^*}{\partial y}+w_1^*\frac{\partial u_1^*}{\partial z}+u_1^*\frac{\partial w_1^*}{\partial z}.$$

Now integrating over the width and using the Leibnitz integral rule for integrals with constant boundaries results in

$$\frac{1}{2B}\left(\frac{\partial}{\partial t}\int_{-B}^{B}u_1^*\,\mathrm{d}y+\frac{\partial}{\partial x}\int_{-B}^{B}\left(u_1^*\right)^2\mathrm{d}y+\left[v_1^*u_1^*\right]_{-B}^{B}+\frac{\partial}{\partial z}\int_{-B}^{B}w_1^*u_1^*\,\mathrm{d}y\right). \tag{2.8}$$

Again the boundary condition that the side walls are impermeable, i.e. $v^*=0$ at $y=\pm B$ is used to eliminate $\left[v_1^*u_1^*\right]_{-B}^{B}$.

The two terms with integrals of products are further elaborated by decomposing the velocities u_1^* and w_1^* into a width-averaged part and a fluctuating part. The notation for width-averaged variables as given by Eq. (2.2) is used and the fluctuating parts are denoted by u_1' and w_1'. This definition yields the properties that u_1 and w_1 are independent of y, and that the width-average of the fluctuating part is zero, i.e. $\int_{-B}^{B}u_1'\,\mathrm{d}y=0$. Using this notation the terms with integrals of products can be rewriten as

$$\frac{1}{2B}\frac{\partial}{\partial x}\int_{-B}^{B}\left(u_1^*\right)^2\mathrm{d}y+\frac{1}{2B}\frac{\partial}{\partial z}\int_{-B}^{B}w_1^*u_1^*\,\mathrm{d}y=\frac{1}{2B}\frac{\partial}{\partial x}\left(2B\cdot u_1^2+\int_{-B}^{B}u_1'^2\mathrm{d}y\right)+\frac{1}{2B}\frac{\partial}{\partial z}\left(2B\cdot u_1w_1+\int_{-B}^{B}u_1'w_1'\mathrm{d}y\right).$$

The effects of the correlation of the fluctuating parts in the integrals are assumed to act as effective diffusive contributions and are parameterised as eddy viscosity terms, using the following assumption:

$$\int_{-B}^{B}u_1'^2\mathrm{d}y=-2B\cdot A_h'\frac{\partial u_1}{\partial x},\qquad\qquad\int_{-B}^{B}u_1'w_1'\mathrm{d}y=-2B\cdot A_v'\frac{\partial u_1}{\partial z}.$$

This results in the following expression for the two integrals of products:

$$\frac{\partial u_1^2}{\partial x}+\frac{\partial}{\partial x}\left(-A_h'\frac{\partial u_1}{\partial x}\right)+\frac{\partial u_1w_1}{\partial z}+\frac{\partial}{\partial z}\left(-A_v'\frac{\partial u_1}{\partial z}\right).$$

The product rule for differentiation is used and the continuity equation for the top layer multiplied by u_1 is subtracted. This yields

$$\begin{aligned}2u_1\frac{\partial u_1}{\partial x}+\frac{\partial}{\partial x}\left(-A_h'\frac{\partial u_1}{\partial x}\right)+w_1\frac{\partial u_1}{\partial z}+u_1\frac{\partial w_1}{\partial z}+\frac{\partial}{\partial z}\left(-A_v'\frac{\partial u_1}{\partial z}\right)-u_1\left(\frac{\partial u_1}{\partial x}+\frac{\partial w_1}{\partial z}\right)\\ =u_1\frac{\partial u_1}{\partial x}+w_1\frac{\partial u_1}{\partial z}+\frac{\partial}{\partial x}\left(-A_h'\frac{\partial u_1}{\partial x}\right)+\frac{\partial}{\partial z}\left(-A_v'\frac{\partial u_1}{\partial z}\right).\end{aligned}$$

This result is substituted back into the expression for the left hand side as given by Eq. (2.8), and the notation for the width-averaged variables u_1 and w_1 is again used. This yields the final expression for the left hand side:

$$\frac{\partial u_1}{\partial t} + u_1\frac{\partial u_1}{\partial x} + w_1\frac{\partial u_1}{\partial z} + \frac{\partial}{\partial x}\left(-A'_h\frac{\partial u_1}{\partial x}\right) + \frac{\partial}{\partial z}\left(-A'_v\frac{\partial u_1}{\partial z}\right).$$

Combining the left- and right-hand side now yields the momentum equation for the top layer:

$$\frac{\partial u_1}{\partial t} + u_1\frac{\partial u_1}{\partial x} + w_1\frac{\partial u_1}{\partial z} = -g\frac{\partial \eta}{\partial x} + \frac{\partial}{\partial x}\left(A_h\frac{\partial u_1}{\partial x}\right) + \frac{\partial}{\partial z}\left(A_v\frac{\partial u_1}{\partial z}\right). \tag{2.9}$$

Here $A_v = \tilde{A}_v + A'_v$ and $A_h = \tilde{A}_h + A'_h$.
The momentum equation for the bottom layer is given by:

$$\frac{\partial u_2}{\partial t} + u_2\frac{\partial u_2}{\partial x} + w_2\frac{\partial u_2}{\partial z} = -g\frac{\partial \zeta}{\partial x} - g\frac{\rho_1}{\rho_2}\left(\frac{\partial \eta}{\partial x} - \frac{\partial \zeta}{\partial x}\right) + \frac{\partial}{\partial x}\left(A_h\frac{\partial u_2}{\partial x}\right) + \frac{\partial}{\partial z}\left(A_v\frac{\partial u_2}{\partial z}\right). \tag{2.10}$$

2.4. Boundary conditions for the width-averaged model

The free surface elevation at $x = 0$, where the embayment is connected to the ocean, is forced by the fluctuations of the tide, yielding the tidal forcing boundary condition:

$$\eta = A\cos(\sigma t) \qquad \text{at } x = 0. \tag{2.11}$$

Here A is the amplitude of the tidal oceanic wave, and σ is the tidal frequency. For the semidiurnal tide, the tidal frequency is $1.4\cdot10^{-4}$. The tidal amplitude is assumed to be much smaller then the water depth: $A \ll H$. To focus on the effects of tidal forcing at the surface on the internal dynamics, the amplitude variation of the interface is set to 0 at $x = 0$:

$$\zeta = 0 \qquad \text{at } x = 0. \tag{2.12}$$

This eliminates the influence of forced interface fluctuations by the ocean on the internal dynamics and nonlinear interaction between the effects of the tidal surface forcing and oceanic forcing of the interface.

The coastal boundary is assumed to be impermeable.

$$u = 0 \qquad \text{at } x = L.$$

At the free surface stress due to the wind is assumed to be negligible, therefore a no-stress condition is imposed at the free surface:

$$A_v\frac{\partial u_1}{\partial z} = 0 \qquad \text{at } z = \eta. \tag{2.13}$$

Apart from the no-stress condition, the kinematic boundary condition is imposed at the free surface. This boundary condition dictates that a particle which is located at the surface, will stay at the surface, and reads:

$$w_1 = \frac{\partial \eta}{\partial t} + u_1\frac{\partial \eta}{\partial x} \qquad \text{at } z = \eta. \tag{2.14}$$

At the bottom, a partial slip condition is imposed:

$$A_v\frac{\partial u_2}{\partial z} = s_f u_2 \qquad \text{at } z = -H. \tag{2.15}$$

With s_f the so-called stress parameter. This stress parameter and the eddy viscosity together determine the partial slip parameter: $\frac{s_f}{A_v}$. In figure 1.3 an interpretation of the partial slip parameter is depicted. In this figure the partial slip parameter is denoted by λ. The partial-slip parameter can vary to prescribe different types of bottom-stress. A zero partial-slip parameter corresponds to perfect slip, a large value corresponds to no slip.

Variable	Typical Scale	Dimensionless Expression
t	σ, tidal frequency	$t = \sigma^{-1}\tilde{t}$
ζ,η	A, tidal amplitude	$\zeta = A\tilde{\zeta}, \eta = A\tilde{\eta}$
z, H	H_0, embayment entrance depth	$z = H_0\tilde{z}$, $H = H_0\tilde{H}$
x	L, channel length	$x = L\tilde{x}$
u	$U = \frac{A\sigma L}{H_0}$	$u = U\tilde{u}$
w	$W = \frac{H_0 U}{L}$	$w = W\tilde{w}$

Table 2.1: Variables expressed as their typical scale and associated dimensionless variable

Parameter	Value
σ	$1.4 \cdot 10^{-4}\frac{1}{s}$
g	$9.81\frac{m}{s^2}$
L	$50000m$
H_0	$10m$
A	$1m$
A_v	$0.001\frac{m^2}{s}$
A_h	$10\frac{m^2}{s}$
ρ_1	$998\frac{kg}{m^3}$
ρ_2	$1000\frac{kg}{m^3}$

Table 2.2: Parameters and their typical values

Furthermore the bed is impermeable so flow perpendicular to the bed is required to vanish. This yields the impermeability condition:

$$w_2 = -u_2\frac{\partial H}{\partial x} \qquad \text{at } z = -H. \tag{2.16}$$

At the interface between the two layers of water the flow and the stresses are taken to be continuous. This yields the continuity conditions:

$$u_1 = u_2, \qquad w_1 = w_2, \qquad A_v\frac{\partial u_1}{\partial z} = A_v\frac{\partial u_2}{\partial z}, \qquad A_v\frac{\partial w_1}{\partial z} = A_v\frac{\partial w_2}{\partial z}, \qquad \text{at } z = -h+\zeta. \tag{2.17}$$

Also the two layers are required to stay separated, so two kinematic boundary conditions are imposed:

$$w_1 = \frac{\partial \zeta}{\partial t} + u_1\frac{\partial \zeta}{\partial x}, \qquad w_2 = \frac{\partial \zeta}{\partial t} + u_2\frac{\partial \zeta}{\partial x}, \qquad \text{at } x = -h+\zeta. \tag{2.18}$$

2.5. Scaling

In this section the model equations are scaled to determine the relative importance of each contribution. First all variables are made dimensionless, this result can be used to determine the relative importance of the terms of the continuity- and momentum-equations. The boundary conditions are also scaled. These results finally yield the leading order system of equations.

2.5.1. Scaling the variables

In order to scale the continuity- and momentum- equations, all variables are expressed as the product of their typical scale and a dimensionless variable. For example $x = L\cdot\tilde{x}$, where the embayment length L is the typical scale of the spatial variable x, and $\tilde{x}$ is the associated dimensionless variable. In table 2.1 variables and their typical scales are given.
These typical-scale expressions are substituted into the continuity- and momentum-equations. Subsequently, the magnitude of all terms in each equation is related to an order of ϵ, where ϵ is defined as $\epsilon = \frac{A}{H_0}$.

The typical scale for the velocity in the x-direction, U, is determined by integrating the width-averaged continuity equation over the depth of the channel and requiring the contributions of both terms to be ap-

proximately equal:

$$\int_{-H}^{\eta} \frac{\partial u}{\partial x} + \frac{\partial w}{\partial z} \mathrm{d}z = 0$$

$$\int_{-H}^{\zeta} \frac{\partial u_2}{\partial x} + \frac{\partial w_2}{\partial z} \mathrm{d}z + \int_{\zeta}^{\eta} \frac{\partial u_1}{\partial x} + \frac{\partial w_1}{\partial z} \mathrm{d}z = 0$$

$$\frac{\partial}{\partial x}\int_{-H}^{\zeta} u_2 \mathrm{d}z - u_2 \frac{\partial \zeta}{\partial x}\bigg|_{z=\zeta} - u_2 \frac{\partial H}{\partial x}\bigg|_{z=-H} + [w_2]_{-H}^{\zeta} +$$

$$\frac{\partial}{\partial x}\int_{\zeta}^{\eta} u_1 \mathrm{d}z - u_1 \frac{\partial \eta}{\partial x}\bigg|_{z=\eta} + u_1 \frac{\partial \zeta}{\partial x}\bigg|_{z=\zeta} + [w_1]_{\zeta}^{\eta} = 0$$

$$\frac{\partial}{\partial x}\int_{-H}^{\eta} u \mathrm{d}z + \frac{\partial \eta}{\partial t} = 0$$

In the derivation above the Leibnitz integral rule is used, as well as the bottom no-flow boundary condition (Eq. (2.16)), the interface kinematic boundary conditions (Eq. (2.18)) and the surface kinematic boundary condition (Eq. (2.14)). Next the variables are expressed as the product of their typical scale and a dimensionless variable (as given in table 2.1):

$$\frac{U H_0}{L} \frac{\partial}{\partial \tilde{x}} \int_{-H_0 \tilde{H}}^{A\tilde{\eta}} \tilde{u} \mathrm{d}z + \frac{A}{\sigma^{-1}} \frac{\partial \tilde{\eta}}{\partial \tilde{t}} = 0.$$

Requiring the the relative importance of both terms to be equal yields $U = \frac{A\sigma L}{H_0}$
The typical scale for the velocity in the z-direction, W, is now determined using the width-averaged continuity equation:

$$\frac{U}{L}\frac{\partial \tilde{u}}{\partial \tilde{x}} + \frac{W}{H_0}\frac{\partial \tilde{w}}{\partial \tilde{z}} = 0.$$

Again requiring the relative importance of both terms to be equal, it is found that $W = \frac{H_0 U}{L}$.

In table 2.2 the typical values for parameters used in model computations in this paper are given. With these values $\epsilon = 0.1$.

2.5.2. Scaling the continuity equation

The continuity equation is scaled using the dimensionless expressions for all variables as given by table 2.1:

$$\frac{A\sigma L}{H_0 L}\frac{\partial \tilde{u}}{\partial \tilde{x}} + \frac{A\sigma}{H_0}\frac{\partial \tilde{w}}{\partial \tilde{z}} = 0$$

$$\underbrace{\frac{\partial \tilde{u}}{\partial \tilde{x}}}_{\mathcal{O}(1)} + \underbrace{\frac{\partial \tilde{w}}{\partial \tilde{z}}}_{\mathcal{O}(1)} = 0$$

2.5.3. Scaling the momentum equation

The scaled momentum-equation for the top layer is given by:

$$\frac{A\sigma L}{H_0 \cdot \sigma^{-1}}\frac{\partial \tilde{u_1}}{\partial \tilde{t}} + \frac{A^2\sigma^2 L^2}{H_0^2 L}\tilde{u_1}\frac{\partial \tilde{u_1}}{\partial \tilde{x}} + \frac{A^2\sigma^2 L}{H_0^2}\tilde{w_1}\frac{\partial \tilde{u_1}}{\partial \tilde{z}} = -g\frac{A}{L}\frac{\partial \tilde{\eta}}{\partial \tilde{x}} + A_h\frac{A\sigma L}{H_0 L^2}\frac{\partial^2 \tilde{u_1}}{\partial \tilde{x}^2} + A_v\frac{A\sigma L}{H_0^3}\frac{\partial^2 \tilde{u_1}}{\partial \tilde{z}^2}$$

$$\underbrace{\frac{\partial \tilde{u_1}}{\partial \tilde{t}}}_{\mathcal{O}(1)} + \underbrace{\frac{A}{H_0}\tilde{u_1}\frac{\partial \tilde{u_1}}{\partial \tilde{x}}}_{\mathcal{O}(\epsilon)} + \underbrace{\frac{A}{H_0}\tilde{w_1}\frac{\partial \tilde{u_1}}{\partial \tilde{z}}}_{\mathcal{O}(\epsilon)} = -\underbrace{g\frac{H_0}{\sigma^2 L^2}\frac{\partial \tilde{\eta}}{\partial \tilde{x}}}_{\mathcal{O}(1)} + \underbrace{A_h\frac{1}{\sigma L^2}\frac{\partial^2 \tilde{u_1}}{\partial \tilde{x}^2}}_{\mathcal{O}(\epsilon^5)} + \underbrace{A_v\frac{1}{\sigma H_0^2}\frac{\partial^2 \tilde{u_1}}{\partial \tilde{z}^2}}_{\mathcal{O}(1)}$$

The order of each term is determined by calculating the dimensionless coefficient using the typical values form tabel 2.2. For example $g\frac{H_0}{\sigma^2 L^2} = 2.0$, which is in the order of $\epsilon^0 = 0.1^0 = 1$.
Similarly scaling the momentum-equation for the bottom layer results in:

$$\underbrace{\frac{\partial \tilde{u_2}}{\partial \tilde{t}}}_{\mathcal{O}(1)} + \underbrace{\frac{A}{H_0}\tilde{u_2}\frac{\partial \tilde{u_2}}{\partial \tilde{x}}}_{\mathcal{O}(\epsilon)} + \underbrace{\frac{A}{H_0}\tilde{w_2}\frac{\partial \tilde{u_2}}{\partial \tilde{z}}}_{\mathcal{O}(\epsilon)} = -\underbrace{g\frac{H_0}{\sigma^2 L^2}\frac{\partial \tilde{\zeta}}{\partial \tilde{x}}}_{\mathcal{O}(1)} - \underbrace{g\frac{\rho_1}{\rho_2}\frac{H_0}{\sigma^2 L^2}\left(\frac{\partial \tilde{\eta}}{\partial \tilde{x}} - \frac{\partial \tilde{\zeta}}{\partial \tilde{x}}\right)}_{\mathcal{O}(1)} + \underbrace{A_h\frac{1}{\sigma L^2}\frac{\partial^2 \tilde{u_2}}{\partial \tilde{x}^2}}_{\mathcal{O}(\epsilon^5)} + \underbrace{A_v\frac{1}{\sigma H_0^2}\frac{\partial^2 \tilde{u_2}}{\partial \tilde{z}^2}}_{\mathcal{O}(1)}$$

2.5.4. Scaling the boundary conditions

Lastly the boundary conditions are scaled in the same manner. Starting with the boundary conditions at the embayment-entrance

$$\underbrace{\tilde{\eta}}_{\mathcal{O}(1)} = \underbrace{\cos(\tilde{t})}_{\mathcal{O}(1)} \qquad \text{at } \tilde{x} = 0. \tag{2.19}$$

and

$$\underbrace{\tilde{\zeta}}_{\mathcal{O}(1)} = 0 \qquad \text{at } \tilde{x} = 0. \tag{2.20}$$

The boundary condition that states that the wall is impermeable at the end of the embayment (i.e. $u = 0$ at $x = L$) can no longer be imposed, because the terms with the horizontal eddy viscosity A_h in the momentum equations are of order $\mathcal{O}(\epsilon^5)$ and will therefore not appear in the leading order system. The horizontal eddy viscosity term represents small-scale horizontal processes, omitting this term implies that small-scale variations in u are not resolved. Since in the boundary layer at $x = L$, small-scale variations of u are necessary to satisfy this boundary condition, this boundary condition cannot be satisfied using the leading order system. Instead of imposing this impermeable wall condition, the following, weaker, boundary condition is imposed at $x = L$:

$$\underbrace{\int_{-\tilde{H}}^{\overbrace{\epsilon\tilde{\eta}}^{\mathcal{O}(\epsilon)}} \tilde{u}\,\mathrm{d}z}_{\mathcal{O}(1)} = 0 \qquad \text{at } \tilde{x} = 1. \tag{2.21}$$

This boundary condition dictates that the total depth-integrated flow, i.e. the total flow trough the fixed wall, is zero.

The boundary conditions at the surface ($z = \eta$) are linearized around $\tilde{z} = 0$ using a Taylor expansion. This yields

$$\underbrace{A_v \frac{\partial \tilde{u}_1}{\partial \tilde{z}}}_{\mathcal{O}(1)} + \underbrace{A_v \epsilon \tilde{\eta} \frac{\partial^2 \tilde{u}_1}{\partial \tilde{z}^2}}_{\mathcal{O}(\epsilon)} + \text{HOT} = 0 \qquad \text{at } \tilde{z} = 0. \tag{2.22}$$

and

$$\underbrace{\tilde{w}_1}_{\mathcal{O}(1)} + \underbrace{\epsilon\tilde{\eta}\frac{\partial \tilde{w}_1}{\partial \tilde{z}}}_{\mathcal{O}(\epsilon)} + \text{HOT} = \underbrace{\frac{\partial \tilde{\eta}}{\partial \tilde{t}}}_{\mathcal{O}(1)} + \epsilon \underbrace{\left(\tilde{u}_1 + \underbrace{\epsilon\tilde{\eta}\frac{\partial \tilde{u}_1}{\partial \tilde{z}}}_{\mathcal{O}(\epsilon^2)} \right)}_{\mathcal{O}(\epsilon)} \frac{\partial \tilde{\eta}}{\partial \tilde{x}} + \text{HOT} \qquad \text{at } \tilde{z} = 0. \tag{2.23}$$

Here the acronym 'HOT' means 'higher order terms' in the small parameter ϵ.

The partial slip condition at the bed in dimensionless form reads

$$\frac{\partial \tilde{u}_2}{\partial z} = \frac{H_0 s_f}{A_v} \tilde{u}_2 \qquad \text{at } z = -H. \tag{2.24}$$

The diensionless partial slip condition is not ordered, since $\frac{H_0 s_f}{A_v}$ can vary from 0 to very large to prescribe different types of bottom boundary conditions.

The dimensionless impermeability condition reads

$$\underbrace{\tilde{w}_2}_{\mathcal{O}(1)} = \underbrace{-\tilde{u}_2 \frac{\partial \tilde{H}}{\partial \tilde{x}}}_{\mathcal{O}(1)} \qquad \text{at } \tilde{z} = -\tilde{H}. \tag{2.25}$$

At the interface ($z = -h + \zeta$) the boundary conditions are again linearized using a Taylor expansion around $z = -h$

$$\underbrace{\tilde{u}_1}_{\mathcal{O}(1)} + \underbrace{\epsilon\tilde{\zeta}\frac{\partial \tilde{u}_1}{\partial \tilde{z}}}_{\mathcal{O}(\epsilon)} + \text{HOT} = \underbrace{\tilde{u}_2}_{\mathcal{O}(1)} + \underbrace{\epsilon\tilde{\zeta}\frac{\partial \tilde{u}_2}{\partial \tilde{z}}}_{\mathcal{O}(\epsilon)} + \text{HOT} \quad \underbrace{\tilde{w}_1}_{\mathcal{O}(1)} + \underbrace{\epsilon\tilde{\zeta}\frac{\partial \tilde{w}_1}{\partial \tilde{z}}}_{\mathcal{O}(\epsilon)} + \text{HOT} = \underbrace{\tilde{w}_2}_{\mathcal{O}(1)} + \underbrace{\epsilon\tilde{\zeta}\frac{\partial \tilde{w}_2}{\partial \tilde{z}}}_{\mathcal{O}(\epsilon)} + \text{HOT} \quad \text{at } \tilde{z} = -h, \tag{2.26}$$

$$\underbrace{\frac{\partial \tilde{u_1}}{\partial \tilde{z}}}_{\mathcal{O}(1)} + \underbrace{\epsilon\tilde{\zeta}\frac{\partial^2 \tilde{u_1}}{\partial \tilde{z}^2}}_{\mathcal{O}(\epsilon)} + \text{HOT} = \underbrace{\frac{\partial \tilde{u_2}}{\partial \tilde{z}}}_{\mathcal{O}(1)} + \underbrace{\epsilon\tilde{\zeta}\frac{\partial^2 \tilde{u_2}}{\partial \tilde{z}^2}}_{\mathcal{O}(\epsilon)} + \text{HOT} \quad \underbrace{\frac{\partial \tilde{w_1}}{\partial \tilde{z}}}_{\mathcal{O}(1)} + \underbrace{\epsilon\tilde{\zeta}\frac{\partial^2 \tilde{w_1}}{\partial \tilde{z}^2}}_{\mathcal{O}(\epsilon)} + \text{HOT} = \underbrace{\frac{\partial \tilde{w_2}}{\partial \tilde{z}}}_{\mathcal{O}(1)} + \underbrace{\epsilon\tilde{\zeta}\frac{\partial^2 \tilde{w_2}}{\partial \tilde{z}^2}}_{\mathcal{O}(\epsilon)} + \text{HOT} \quad \text{at } \tilde{z} = -h, \tag{2.27}$$

$$\underbrace{\tilde{w_1}}_{\mathcal{O}(1)} + \underbrace{\epsilon\tilde{\zeta}\frac{\partial \tilde{w_1}}{\partial \tilde{z}}}_{\mathcal{O}(\epsilon)} + \text{HOT} = \underbrace{\frac{\partial \tilde{\zeta}}{\partial \tilde{t}}}_{\mathcal{O}(1)} + \epsilon\underbrace{\tilde{u_1}}_{\mathcal{O}(\epsilon)} + \underbrace{\epsilon\tilde{\zeta}\frac{\partial \tilde{u_1}}{\partial \tilde{z}}}_{\mathcal{O}(\epsilon^2)}\frac{\partial \tilde{\zeta}}{\partial \tilde{x}} + \text{HOT} \quad \underbrace{\tilde{w_2}}_{\mathcal{O}(1)} + \underbrace{\epsilon\tilde{\zeta}\frac{\partial \tilde{w_2}}{\partial \tilde{z}}}_{\mathcal{O}(\epsilon)} + \text{HOT} = \underbrace{\frac{\partial \tilde{\zeta}}{\partial \tilde{t}}}_{\mathcal{O}(1)} + \epsilon\underbrace{\tilde{u_2}}_{\mathcal{O}(\epsilon)} + \underbrace{\epsilon\tilde{\zeta}\frac{\partial \tilde{u_2}}{\partial \tilde{z}}}_{\mathcal{O}(\epsilon^2)}\frac{\partial \tilde{\zeta}}{\partial \tilde{x}} + \text{HOT} \tag{2.28}$$

$$\text{at } \tilde{z} = -h.$$

2.6. Leading order system

In the previous sections the continuity-, momentum-equations and boundary conditions were made dimensionless, allowing for the identification of the leading order balances in terms of the small parameter ϵ. Next, the solutions for u, w, ζ and η are approximated by an asymptotic expansion in the parameter ϵ:

$$\begin{aligned} u &= u^0 + \epsilon u^1 + \epsilon^2 u^2 + \cdots \\ w &= w^0 + \epsilon w^1 + \epsilon^2 w^2 + \cdots \\ \zeta &= \zeta^0 + \epsilon\zeta^1 + \epsilon^2\zeta^2 + \cdots \\ \eta &= \eta^0 + \epsilon\eta^1 + \epsilon^2\eta^2 + \cdots \end{aligned}$$

2.6.1. Leading order system

The systems at different orders in ϵ can be obtained by collecting like powers of ϵ in the scaled continuity- and momentum-equations. The leading order system consists of terms of order $\mathcal{O}(1)$, and reads for the continuity equation as

$$\frac{\partial u^0}{\partial x} + \frac{\partial w^0}{\partial z} = 0, \tag{2.29}$$

for the leading order momentum equation for the top layer as

$$\frac{\partial u_1^0}{\partial t} = -g\frac{\partial \eta^0}{\partial x} + A_v\frac{\partial^2 u_1^0}{\partial z^2}, \tag{2.30}$$

and for the leading order momentum equation for the bottom layer as

$$\frac{\partial u_2^0}{\partial t} = -g\frac{\partial \zeta^0}{\partial x} - g\frac{\rho_1}{\rho_2}\left(\frac{\partial \eta^0}{\partial x} - \frac{\partial \zeta^0}{\partial x}\right) + A_v\frac{\partial^2 u_2^0}{\partial z^2}. \tag{2.31}$$

The leading order boundary conditions read

$$\eta^0 = A\cos(\sigma t) \qquad \text{at } x = 0, \tag{2.32}$$

$$\zeta^0 = 0 \qquad \text{at } x = 0, \tag{2.33}$$

$$\int_{-H}^{0} u^0 \mathrm{d}z = 0 \qquad \text{at } x = L, \tag{2.34}$$

$$A_v\frac{\partial u_1^0}{\partial z} = 0 \qquad \text{at } z = 0, \tag{2.35}$$

$$w_1^0 = \frac{\partial \eta^0}{\partial t} \qquad \text{at } z = 0, \tag{2.36}$$

$$A_v \frac{\partial u_2^0}{\partial z} = s_f u_2^0 \qquad \text{at } z = -H, \tag{2.37}$$

$$w_2^0 = -u_2^0 \frac{dH}{dx} \qquad \text{at } x = -H, \tag{2.38}$$

$$u_1^0 = u_2^0 \qquad w_1^0 = w_2^0 \qquad \text{at } x = -h, \tag{2.39}$$

$$\frac{\partial u_1^0}{\partial z} = \frac{\partial u_2^0}{\partial z} \qquad \frac{\partial w_1^0}{\partial z} = \frac{\partial w_2^0}{\partial z} \qquad \text{at } z = -h, \tag{2.40}$$

$$w_1^0 = \frac{\partial \zeta^0}{\partial t} \qquad w_2^0 = \frac{\partial \zeta^0}{\partial t} \qquad \text{at } z = -h. \tag{2.41}$$

2.6.2. The leading order depth-averaged continuity equation

In this section the leading order depth-averaged continuity equations are derived for each layer as they will be used to solve the system of equations.
Taking the depth-integral of the leading order continuity equation for the bottom layer yields:

$$\int_{-H}^{-h} \frac{\partial u_2^0}{\partial x} + \frac{\partial w_2^0}{\partial z} \mathrm{d}z = 0.$$

Now the Leibnitz integral rule is used:

$$\frac{\partial}{\partial x} \int_{-H}^{-h} u_2^0 \mathrm{d}z - u_2^0 \frac{\partial H}{\partial x}\bigg|_{z=-H} + \left[w_2^0 \right]_{-H}^{-h} = 0$$

Using the kinematic boundary condition at the interface, Eq. (2.41) and the impermeability of the bed, Eq. (2.38) yields the leading order depth-averaged continuity equation for the bottom layer:

$$\frac{\partial}{\partial x} \int_{-H}^{-h} u_2^0 \mathrm{d}z + \frac{\partial \zeta^0}{\partial t} = 0 \tag{2.42}$$

The leading order depth-averaged continuity equation for the top layer is derived in a similar fashion, using the Leibnitz integral rule and the kinematic boundary conditions at the interface and free surface (Eq. 2.41 and Eq. 2.36). This yields the leading order depth-averaged continuity equation for the top layer:

$$\begin{aligned} \int_{-h}^{0} \frac{\partial u_1^0}{\partial x} + \frac{\partial w_1^0}{\partial z} \mathrm{d}z &= 0 \\ \frac{\partial}{\partial x} \int_{-h}^{0} u_1^0 \mathrm{d}z + \left[w_1^0 \right]_{-h}^{0} &= 0 \\ \frac{\partial}{\partial x} \int_{-h}^{0} u_1^0 \mathrm{d}z + \frac{\partial \eta^0}{\partial t} - \frac{\partial \zeta^0}{\partial t} &= 0 \end{aligned} \tag{2.43}$$

2.6.3. Solving the leading order system

In this section a brief summary of the methods used to solve the leading order system is given. A more detailed description can be found in appendix A.
Since the system is linear and forced by periodic tidal oscillations, the time-like behavior of the solutions will also be periodic. This means the solutions can be written in the following form:

$$u^0 = \Re(U e^{i\sigma t}), \qquad w^0 = \Re(W e^{i\sigma t}), \qquad \eta^0 = \Re(E e^{i\sigma t}), \qquad \zeta^0 = \Re(Z e^{i\sigma t}). \tag{2.44}$$

Here $U(x,z)$, $W(x,z)$, $E(x)$ and $Z(x)$ are the complex amplitudes that describe the space-like behavior of the solutions. Substituting these expressions into the leading order momentum equations, Eq. (2.30) and Eq. (2.31), yields partial differential equations that can be solved to find expressions for U_1 and U_2. These expressions contain integration constants (these constants appear after integration over z, and may thus still

be functions of x) and the unknown functions $\frac{dE}{dx}$ and $\frac{dZ}{dx}$.
These integration constants follow from the no-stress boundary condition at the free surface (Eq. 2.35), the continuity boundary conditions at the interface (Eq. 2.39 and Eq. 2.40) and the partial slip boundary condition at the bottom (Eq. 2.37), giving expressions for U_1 and U_2 that still depend on the unknown functions $\frac{dE}{dx}$ and $\frac{dZ}{dx}$:

$$U_1 = c_1 e^{rz} + c_2 e^{-rz} - \frac{g}{i\sigma}\frac{dE}{dx} \qquad U_2 = c_3 e^{rz} + c_4 e^{-rz} - \frac{g}{i\sigma}\left(1 - \frac{\rho_1}{\rho_2}\right)\frac{dZ}{dx} - \frac{g}{i\sigma}\frac{\rho_1}{\rho_2}\frac{dE}{dx},$$

with c_1, c_2, c_3 and c_4 the known integration constants and $\frac{dE}{dx}$ and $\frac{dZ}{dx}$ the pressure terms that still need to be solved.
Substituting U_1 and U_2 in the leading order depth-averaged continuity equations yields a system of coupled ordinary differential equations for E and Z:

$$\begin{aligned} T_1\frac{d^2Z}{dx^2} + T_2\frac{d^2E}{dx^2} + T_3\frac{dZ}{dz} + T_4\frac{dE}{dx} - i\sigma Z + i\sigma E = 0 \\ R_1\frac{d^2Z}{dx^2} + R_2\frac{d^2E}{dx^2} + R_3\frac{dZ}{dz} + R_4\frac{dE}{dx} + i\sigma Z = 0, \end{aligned}$$

with T_1, T_2, T_3, T_4, R_1, R_2, R_3 and R_4 known constants. These coupled equations can be solved when $\rho_1 \neq \rho_2$ and $h \neq 0$ and $h \neq H$. A numerical second-order finite difference scheme is used to solve the system.
Solutions for E and Z are numerically differentiated to also obtain solutions for U_1 and U_2. Again a second-order finite difference scheme is used.
The solutions are validated by comparing the case $\rho_1 \approx \rho_2$ to solutions from Dijkstra et al. (2017).

3

Results

In this chapter results obtained with the model derived in the previous chapter are presented. First the basic properties of ζ^0, η^0 and u^0 and the properties of the two-layer system are examined. Then the effects of the partial slip condition and the variable bed are studied.

3.1. Reference case

In the reference case typical values for the parameters, as given by table 3.1 are used. The bed is taken to be invariant, so the undisturbed water depth is equal to H_0 everywhere.

In figure 3.1, the free surface η^0 and the interface ζ^0 are plotted at different moments in time. All subplots have the same axes, with vertical coordinate z on the vertical axis, and on the horizontal axis is the location in the embayment, denoted by x. In each subplot the solid line represents the free surface η^0 and the dashed line represents ζ^0.
At $x = 0$, the variation of the free surface is prescribed by the tidal forcing from the ocean (Eq. 2.32). At $t = 0$h, it is high tide and the tidal forcing is at its maximum amplitude, i.e. the free surface is found at $z = A$. As time continues the surface elevation at the ocean decreases, and with it the free surface at the embayment entrance. After 6 hours, at $t = 6$h, it is almost low tide and the surface elevation is near its minimum, $z = -A$. Hereafter the tide turns and the free surface at the entrance starts to rise again.
The interface between the two layers of water is kept fixed at $z = -h$ by prescribing the no-amplitude boundary condition (Eq. 2.33). At high tide, $t = 0$h, the surface elevation at the coastal boundary of the embayment $x = L$, is greater than at the entrance. At low tide, $t = 6$, the free surface at the end of the embayment is lower than at the entrance. The tidal range as prescribed by the oceanic surface fluctuations at the embayment-entrance is amplified throughout the channel and the interface rises and falls along with the free surface over the tidal period.

In figure 3.2 the velocity-component u^0 at different moments in time is depicted using contourplots. As in figure 3.1, all subplots have the same axes with z on the vertical axis and x on the horizontal axis. With flood

Parameter	Value
σ	$1.4 \cdot 10^{-4} s^{-1}$
g	$9.81 ms^{-2}$
L	$50000m$
H_0	$10m$
A	$1m$
A_v	$0.001 m^2 s^{-1}$
s_f	$0.01 ms^{-1}$
ρ_1	$998 kg m^{-3}$
ρ_2	$1000 kg m^{-3}$
h	$2m$

Table 3.1: Default parameter values

Figure 3.1: The free surface η^0 and the interface ζ^0 at different moments in time

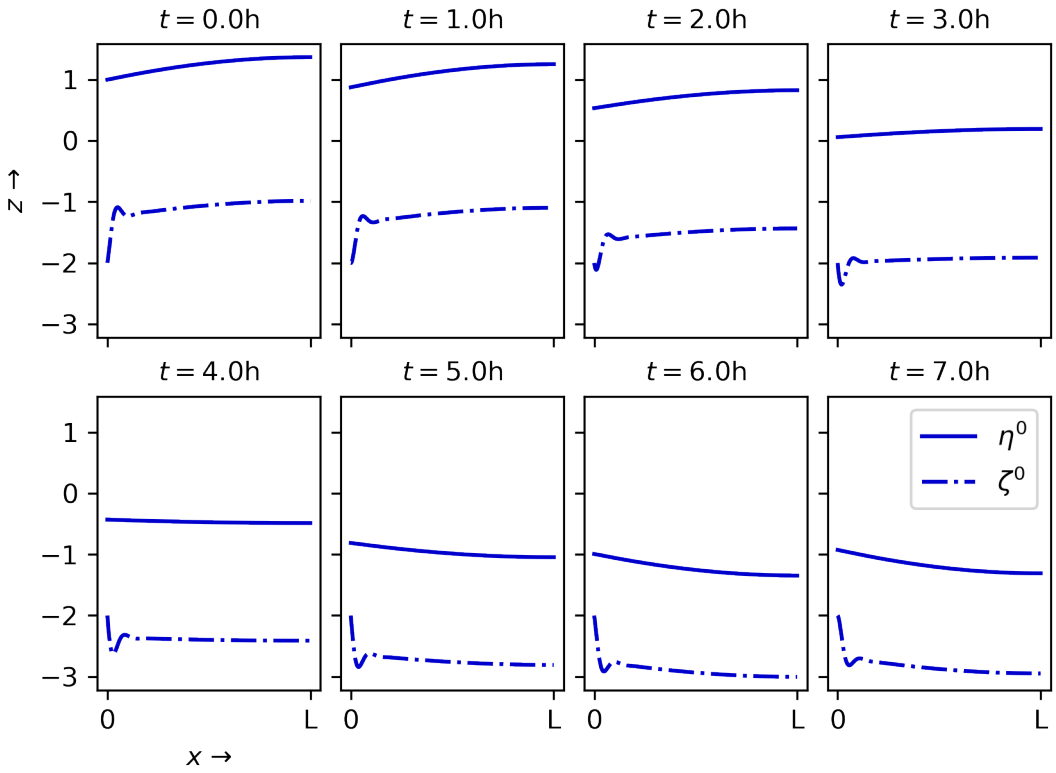

currents, the water flows in the positive x-direction. These conditions are represented by warmer colors, whereas colder colors represent ebb currents, or flow in the negative x-direction. Darker colors correspond to a larger flow velocity.
At $t = 0$h it is high tide and the incoming flood current decays, as the outgoing ebb current appears. As time continous, the ebb current grows stronger and reaches its peak velocity between $t = 3$h and $t = 4$h. At $t = 6$h, low tide is reached and the flood current takes over again.

In figure 3.3 the amplitude of the free surface η^0 and the interface ζ^0 are depicted for different values of ρ_1, with location coordinate x on the horizontal axis and vertical coordinate z on the vertical axis. The bed is taken to be uniform and apart from ρ_1, all variables are given the values in table 2.2. In accordance to observations made by Winant (2010), the interface variations are characterized by smaller wavelengths than the surface. Minor variations in the density ρ_1 have a large effect on the dynamis of interface. When decreasing the density ρ_1 is decreased to 990 from its default value of 998, a change of 0.8%, the root mean square of the amplitude of the interface $|Z|$ changes by 7.9%. Decreasing ρ_1 from its default value by 4.8% to 950 yields a 15.0% change in the root mean square of $|Z|$.

3.2. Partial slip

In this section the effects of the partial slip condition on the resulting water motion are explored.

In the first set of experiments, the partial slip parameter $\frac{s_f}{A_v}$ is varied, while keeping the eddy viscosity A_v fixed at its default value $A_v = 0.001 m^2 s^{-1}$. Three different model solutions are compared where the stress parameter s_f is picked from $s_f = \{0 ms^{-1}, 0.001 ms^{-1}, 0.01 ms^{-1}\}$, such that the partial slip parameter $\frac{s_f}{A_v}$ is varied from 0 to 1 to 10 respectively. All other parameters are kept at their default values, as given by table 2.2, and the bed is taken to be flat. Properties of these solutions are shown in figures 3.4 and 3.5.
In figure 3.4 the velocity-component u^0 is shown as a contourplot, approximately at the midpoint between high- and low-tide ($t = 3$h). All subplots again have the same axes; vertical coordinate z on the vertical axis and position x on the horizontal axis. Colder colors correspond to ebb currents and darker colors represent large velocities.

Figure 3.2: The velocity profile u^0 at different moments in time.

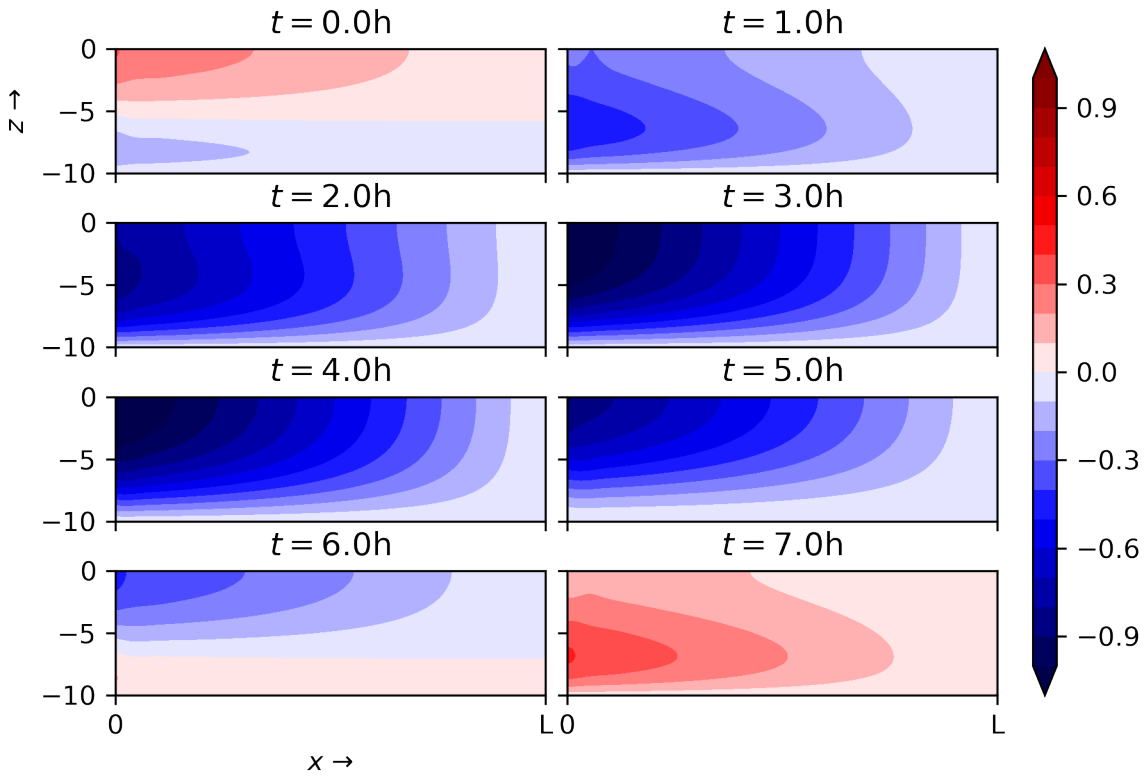

Figure 3.3: The amplitude of the free surface η^0 and the interface ζ^0 for different values of ρ_1

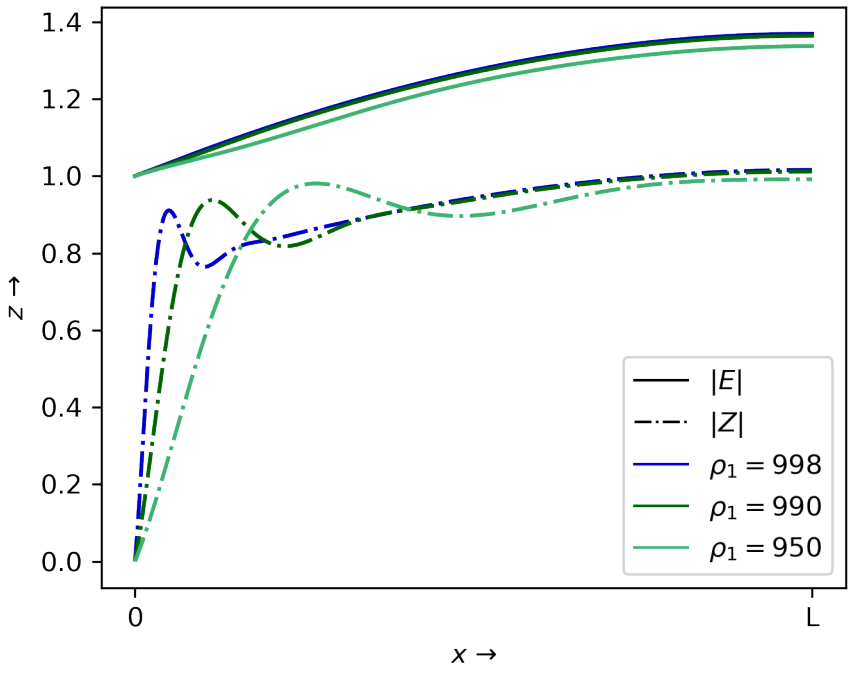

Figure 3.4: The velocity profile u^0 for different values of the partial slip parameter $\frac{s_f}{A_v}$.

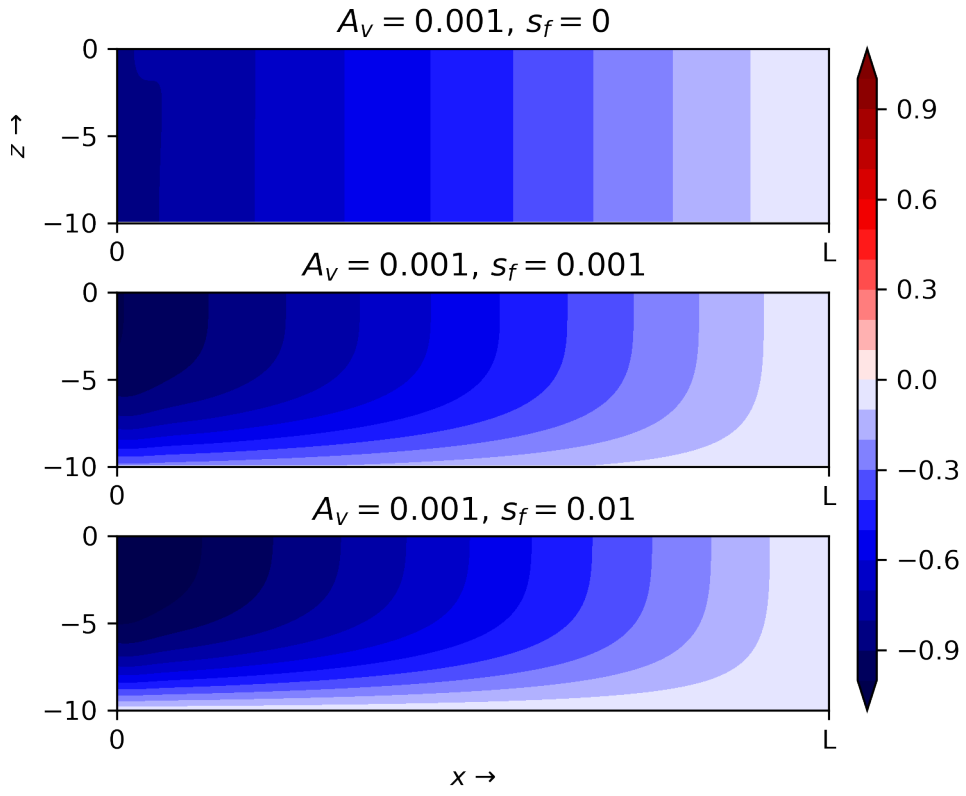

Figure 3.5: The amplitude of the free surface η^0 and the interface ζ^0 for different values of the partial slip parameter $\frac{s_f}{A_v}$

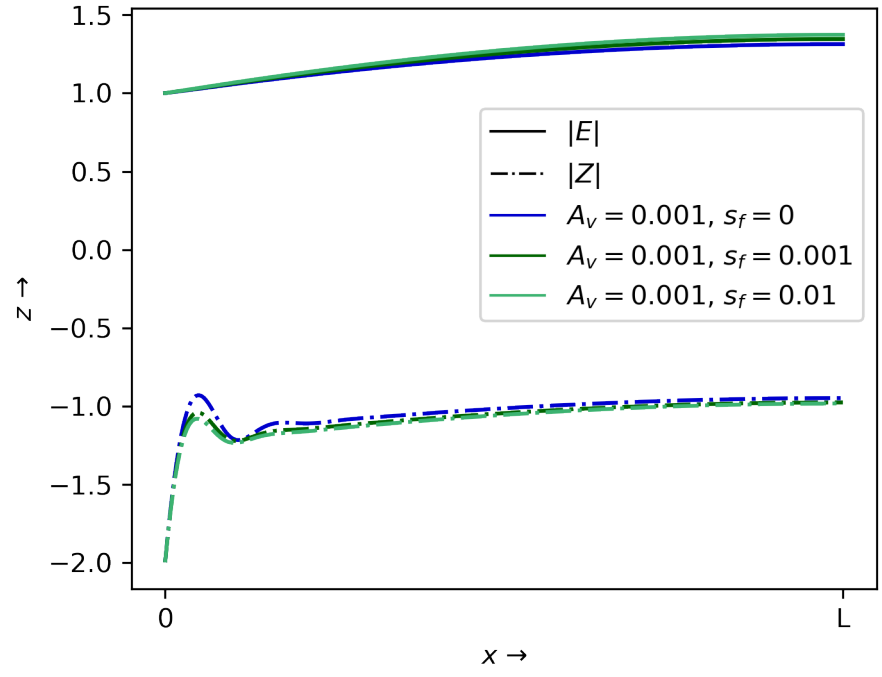

Figure 3.6: The velocity profile u^0 for different values of the eddy viscosity A_v.

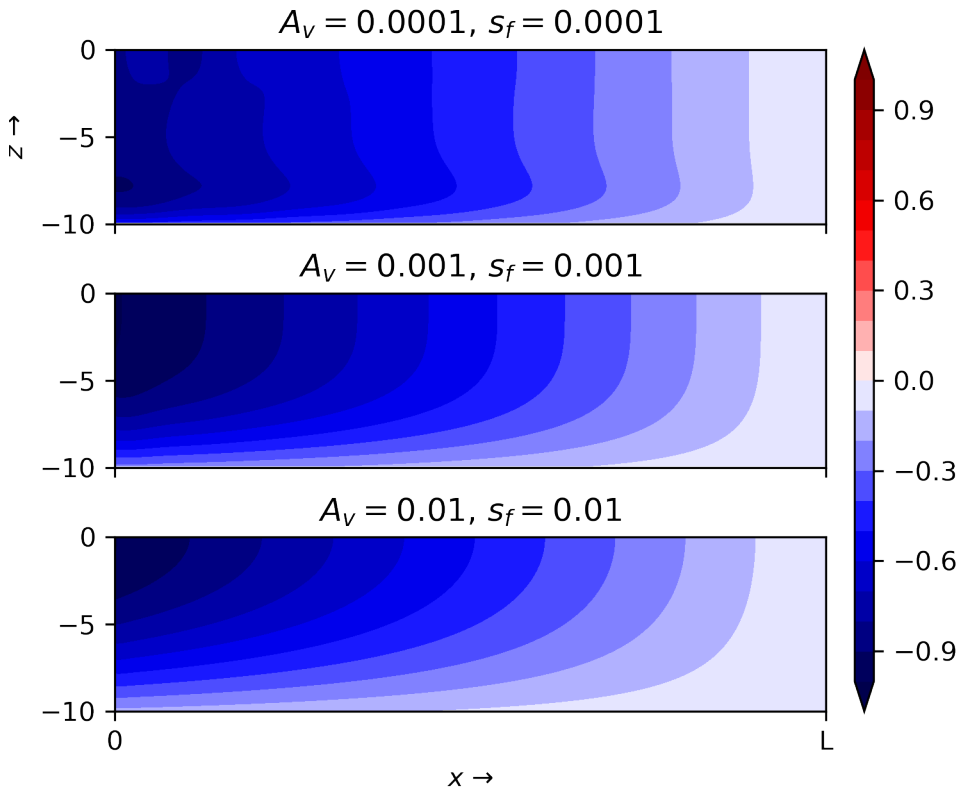

When the partial slip parameter $\frac{s_f}{A_v} = 0$, the velocity profile does not decrease near the bed. As the partial slip parameter increases, the flow velocity near the bed becomes smaller. The flow velocity away from the bed is similar for each stress parameter s_f.
In figure 3.5 the amplitude of the free surface $|E|$ and of the interface $|Z|$ is plotted, with z on the vertical axis, and x on the horizontal axis. Both the amplitude of free surface and of the interface are scarcely affected by the varying bottom stress.

In the next set of model experiments, the partial slip parameter $\frac{s_f}{A_v}$ is kept constant ($\frac{s_f}{A_v} = 1$) by varying the eddy viscosity A_v and the stress parameter s_f simultaneously. Results from these experiments are displayed in figures 3.6 and 3.7
In figure 3.6 for each of these parameter settings, the velocity-component u^0 is depicted as a contourplot, again at the approximate midpoint between high- and low tide (t = 3h). The axes of each subplot denote vertical coordinate z on the vertical axis and position x on the horizontal axis. Colder colors correspond to ebb currents and darker colors represent large velocities. For each of these solutions, the flow velocity near the bed is reduced everywhere. For large values of the viscosity A_v and stress parameter s_f, the velocity away form the bed is also reduced, for low viscosity A_v and s_f, the velocity away form the bed is not reduced. An overshoot is observed in the velocity profile for $A_v = 0.0001$. In figure 3.7 the amplitude of the free surface $|E|$ and of the interface $|Z|$ are plotted, with z on the vertical axis and x on the horizontal axis. The free surface is not changed much by varying A_v and s_f. The interface fluctuates strongly for small viscosity. These fluctuations are dampened by increasing viscosity and their wavelength decreases.

Finally model results for different embayment lengths are compared. Also the eddy viscosity A_v and stress parameter s_f are varied. All other parameters are kept at their typical values (as given by table 2.2) and the bed is taken to be flat.
In figure 3.8 the tidal range at the coastal boundary of the embayment ($x = L$) is plotted for different values of the eddy viscosity A_v and stress parameter s_f. The tidal range is twice the tidal amplitude and is a function of the position x. The axes of each subplot are identical. On the vertical axis is the coastal tidal range, on the horizontal axis the embayment-length L. The solid line represents the tidal range of η^0, the dashed line represents the tidal range of the interface ζ^0.

Figure 3.7: The amplitude of the free surface η^0 and the interface ζ^0 for different values of the partial slip parameter eddy viscosity A_v

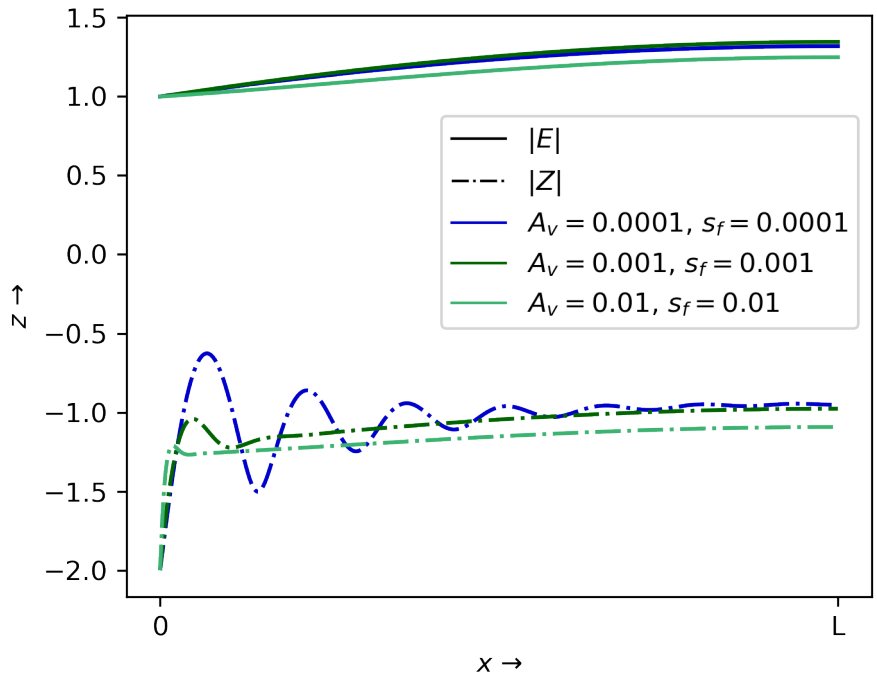

In the first subplot, the eddy viscosity $A_v = 0.001$ and the partial slip parameter $\frac{s_f}{A_v} = 0$. For specific values of the embayment length L, the free surface and the interface experience resonance, and the tidal range is amplified throughout the channel: the tidal range at the coastal boundary of the embayment is far greater than at the entrance.
In the second subplot the eddy viscosity is again $A_v = 0.001$, but the partial slip parameter is $\frac{s_f}{A_v} = 1$. The amplification of the tidal range of the free surface η^0 and the interface ζ^0 is reduced and the embayment-lengths at which resonance occurs decrease.
In the third subplot the eddy viscosity is kept the same as in the second subplot ($A_v = 0.001$), but the partial slip parameter is increased $\frac{s_f}{A_v} = 10$. Compared to the second subplot, the amplification is sightly further reduced, and the resonance lengths are slightly further decreased.
Finally in the fourth subplot, the eddy viscosity is increased to $A_v = 0.01$, and the partial slip parameter is kept the same as in the second subplot ($\frac{s_f}{A_v} = 1$). Compared to the second subplot, the amplification is drasically reduced, also the resonance length is further decreased.

3.3. Variable bed

First three model solutions with different linearly varying bed profiles are compared. The difference in water depth between the embayment-entrance ($x = 0$) and the coastal boundary of the embayment ($x = L$) is denoted by ΔH, and takes on the values 0, 0.5 and 1. All variables are kept at their typical values as given by table 2.2. The results from this experiment are depicted in figures 3.9, 3.10 and 3.11.
In figure 3.9 the depth average of the velocity-component u^0 is plotted over time for different values of ΔH. In figure 3.10 the surface elevation of the associated free surface η^0 is plotted. The axes for each subplot in figures 3.9 and 3.10 are identical, with the horizontal axis denoting the position in the embayment, and the vertical axis the time t. In figure 3.9 colder colors correspond to ebb-flow, warmer colors to flood-flow. Darker colors represent larger flow velocities. In figure 3.10, warmer colors indicate that the free surface is elevated above the undisturbed surface (at $z = 0$) whereas colder colors signify that the free surface has dropped below $z = 0$. Darker colors represent larger deviations from $z = 0$.
When the water depth is constant the tidal dynamics inside the embayment are syncronized with the oceanic tidal forcing. At $t = 0$h the free surface at the embayment entrance is at high-tide, as is the free surface at the

Figure 3.8: The coastal tidal range plotted against the embayment length for different values of eddy viscosity A_v and stress parameter s_f

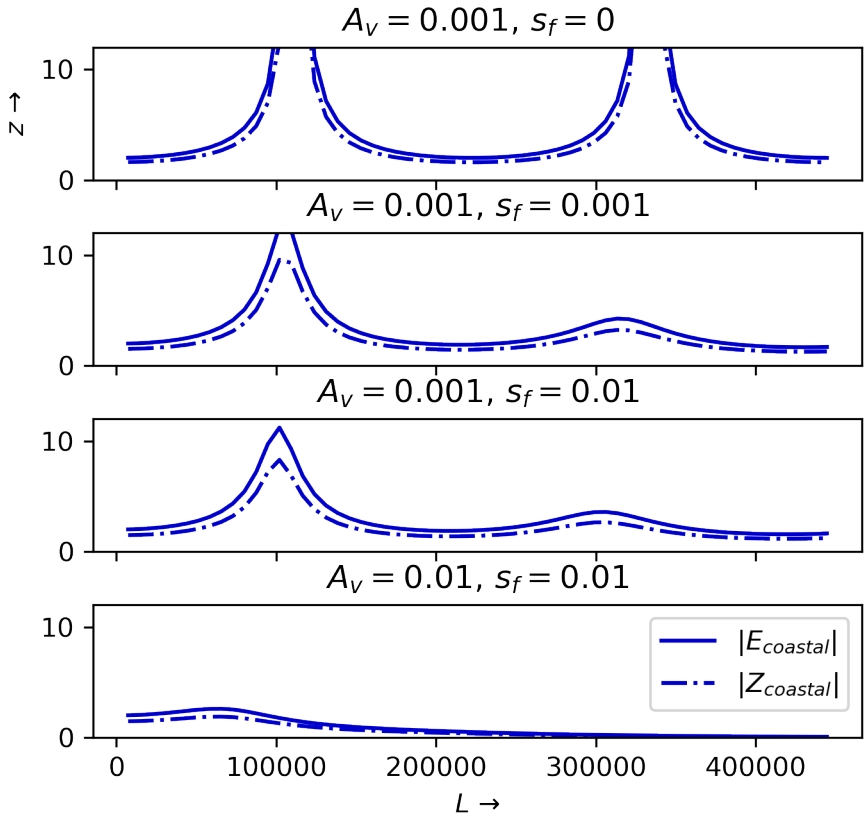

Figure 3.9: Depth averaged velocity u^0 over time for different values of the depth-difference between the embayment-entrance and the coastal end ΔH

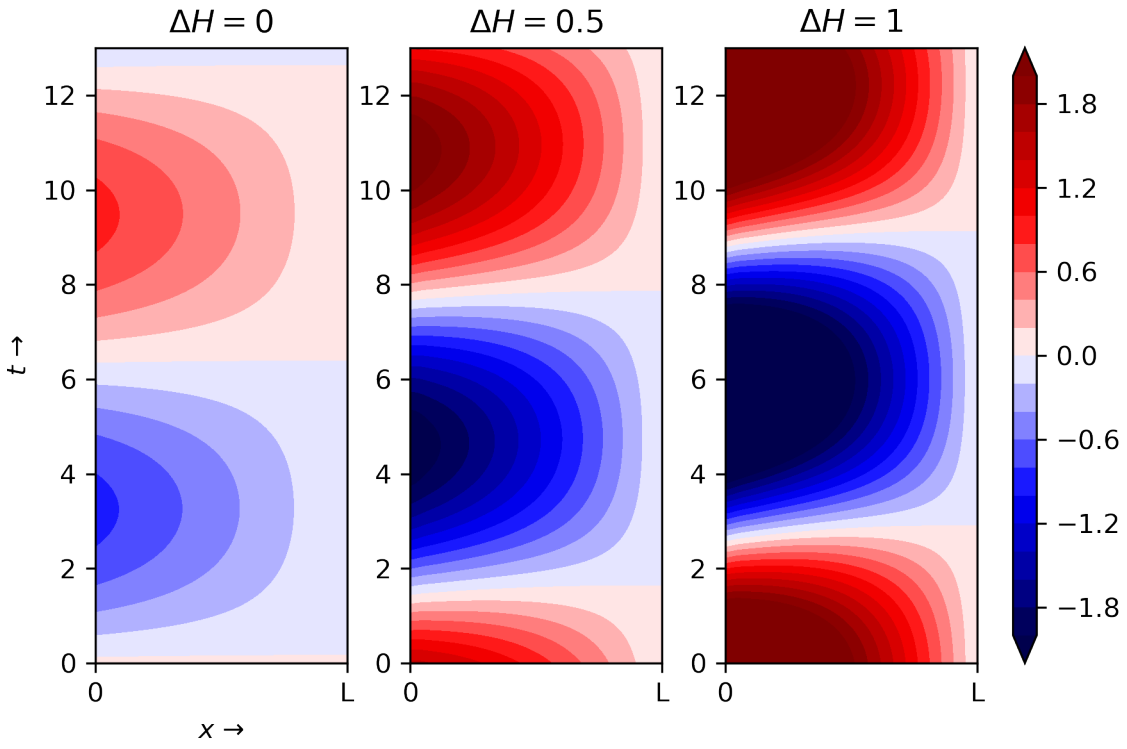

Figure 3.10: Free surface elevation η^0 over time for different values of the depth-difference between the embayment-entrance and the coastal end ΔH

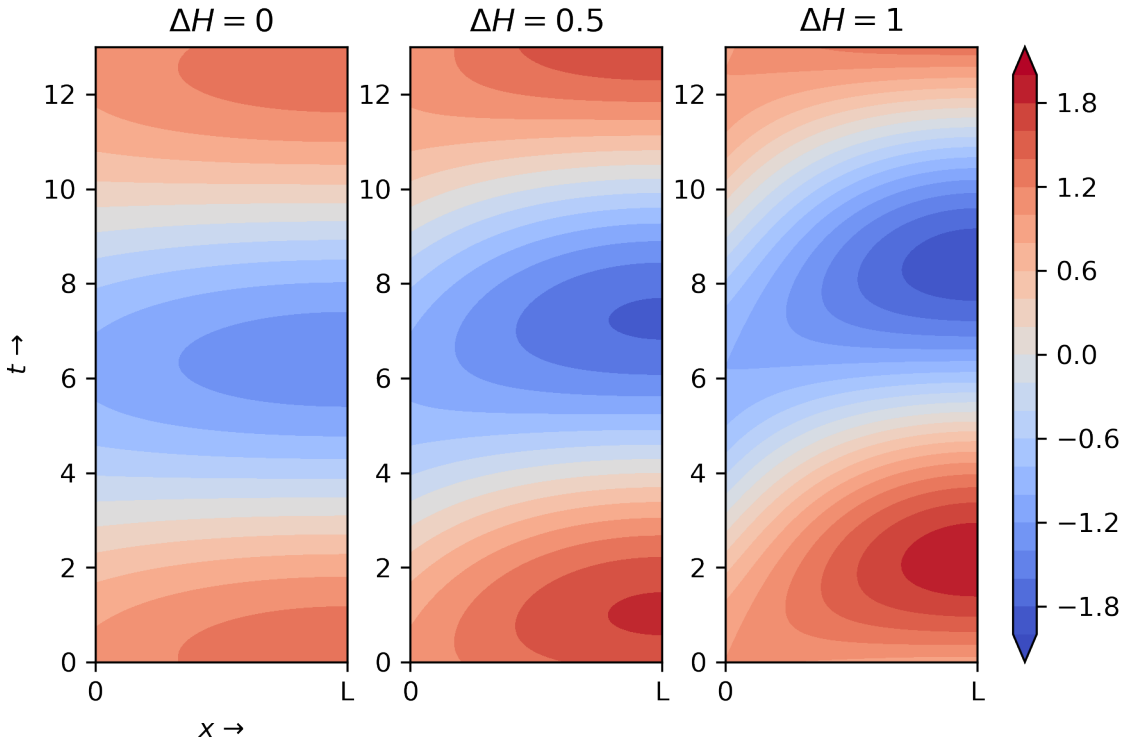

Figure 3.11: The amplitude of the free surface η^0 and the interface ζ^0 for different values of the depth-difference between the embayment-entrance and the coastal end ΔH

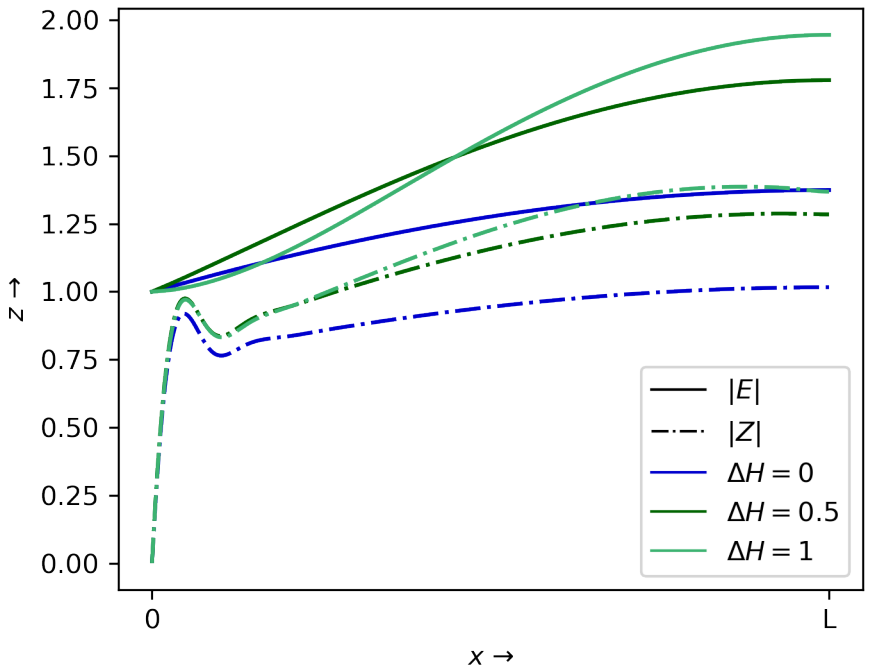

coastal end. At this point the ebb-flow starts. At $t = 6:25$h, the surface elevation is at its minimum for both $x = 0$ and $x = L$, and the flood-flow begins.
As the bed slope is increased, the surface elevation at the coastal end of the embayment starts to lag the tidal forcing at the embayment-entrance: minima and maxima are reached at a later time at the coastal end than at the entrance. The tidal range also increases as the bed slope increases. The flow-current direction-reversal also happens at later time and the overall flow velocity increases, compared to the flat-bed case.
In figure 3.11 the amplitude of the free surface $|E|$ and of the interface $|Z|$ are plotted, with z on the vertical axis and x on the horizontal axis. The amplitude of the free surface is amplified as the water depth difference ΔH increases. This was also observed in figure 3.10. The amplitude of the interface is similarly amplified. The horizontal structure of the fluctuations in the interface is not influenced much by varying ΔH.

Lastly again the tidal range at the coastal boundary of the embayment is plotted against the embayment-length. On the vertical axis is the tidal range at the coastal boundary, and on the horizontal axis the embayment length L. Solutions for several different linearly sloping beds are compared. The solid line depicts the tidal range of the free surface η^0, the dashed line that of the interface ζ^0. The tidal range of the interface at the embayment-entrace is prescribed to be 0. For specific embayment-lengths, the tidal ranges of the free surface and interface experience resonance. They are amplified througout the embayment, and are much larger at the coastal boundary than at the entrance.
These resonance characteristics are somewhat dampened by an increasing bed-slope. Also the embayment-lenghts at which resonance occurs decrease.
Figures 3.9 and 3.10 apply to solutions where the embayment-length is 50000m. For this length, the embayment is closer to resonance when the bed is inclined. This is in accordance with the observed increased tidal range in figure 3.10 and 3.11 and the increased overall flow velocity in figure 3.9.

Figure 3.12: The coastal tidal range plotted against the embayment length for different values of the depth-difference between the embayment-entrance and coastal end ΔH.

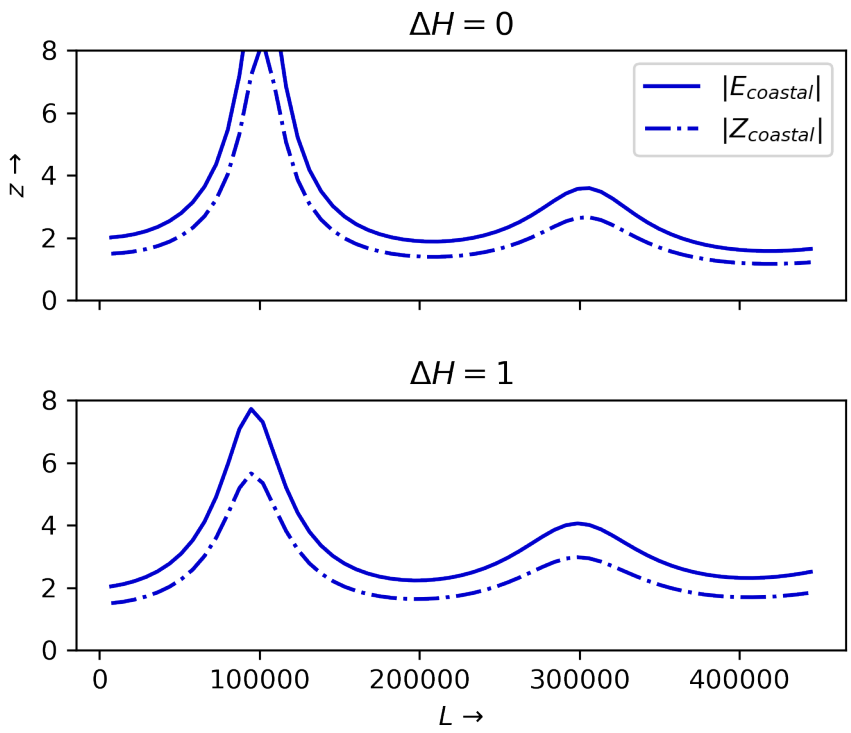

4

Conclusion and discussion

In this thesis, a width-averaged model of tidal dynamics in an idealized stratified embayment is derived. The two layers are assumed to stay completely separated, and are divided by an interface. The density within each layer is taken to be constant. The bottom stress is modeled by a partial slip condition, and the bed profile is allowed to vary over the length of the embayment. The length of the embayment is assumed to be much larger than the typical water depth, and the depth is assumed to be much larger than the amplitudes of the free surface and interface.
The effects of tidal forcing of the free surface on the internal dynamics are investigated. To this end, the free surface at the embayment entrance is prescribed to follow tidal fluctuations at the ocean, while the amplitude of the interface is kept fixed at zero. In order to solve the model a scaling analysis is applied. After scaling the equations, the relative magnitude of different terms of each equation is determined using the small parameter ϵ, the ratio of the free surface amplitude and the water depth. The model yields solutions for the free surface η, the interface ζ and the horizontal velocity component u.
In accordance with Winant (2010), the dynamics of the interface are characterized by smaller scale horizontal fluctuations those at than the free surface. Furthermore, resonance can be observed. For specific embayment lengths, the free surface amplitude is strongly amplified. These resonance characteristics are also observed in this thesis. Near resonance, the assumption that the amplitude is much smaller than the water depth is violated. Further research is needed to show how the water motions behave close to resonance. Finally Winant (2010) found the model solutions to be highly sensitive to variations in the densities of the two layers. This observation has been confirmed by the model developed in this thesis. The model in this thesis is developed as an extension of the model developed by Winant (2010). The bottom stress is parameterized as partial slip (as opposed to no slip in Winant (2010)), so that the bottom stress can be varied. This model also allows for level variations of the bed. These extensions have offered two research questions which will now be answered. The first question posed in this thesis is:

1. How does bottom stress affect the internal tides in a stratified tidal basin?

The flow velocity at the bottom of the embayment is slowed down by increasing the partial slip parameter $\frac{s_f}{A_v}$. Increased viscosity A_v also dampens flow velocity further away from the bed. For small viscosity, an overshoot is observed in the velocity profile. The partial slip parameter does not influence the horizontal structure of fluctuations in the interface much. Increased viscosity however, dampens fluctuations of the interface. The wavelength of these fluctuations becomes smaller with increasing viscosity. Resonance characteristics in the internal tides of the embayment are somewhat dampened by increased bottom stress (i.e. increased partial slip parameter). Increasing the viscosity A_v has a larger dampening effect on the resonance. Resonance also occurs at smaller embayment lengths.
The second question posed in this thesis is:

2. How does a variable bed affect the internal tides in a stratified basin?

An increasing slope of the embayment bed yields a lag in the ebb and flood currents and high and low tide at the end of the embayment with respect to the oceanic tides. The horizontal structure of the interface fluctuations is not influenced much by the bed slope. The resonance peaks are somewhat dampened by an

increasing slope and the resonance lengths are slightly decreased.
In this model level variations of the bed are allowed, however the ratio of free surface amplitude and the water depth is required to be small. Also the depth of the undisturbed interface is not allowed to vary. Further research is needed to develop a model that allows the water depth to be of the same scale as the free surface amplitude the undisturbed interface depth to vary.
Further research is also needed to investigate the overshoot observed in the velocity profile for small viscosity. Since the horizontal eddy viscosity term in the momentum equation is omitted in the leading order system, small horizontal scale variations are not solved by the model in this thesis. As viscosity decreases, smaller wavelength fluctuations in the interface appear. The behavior of these fluctuations can be investigated in more detail using a model that explicitly solves small horizontal scale variations.

A

Appendix

In this appendix a more detailed description of the methods used to solve the leading order system of equations is given. First the leading order equations are stated again for overview. Then the system is solved.
The leading order continuity equation:

$$\frac{\partial u^0}{\partial x} + \frac{\partial w^0}{\partial z} = 0 \tag{A.1}$$

The leading order momentum equation for the top layer:

$$\frac{\partial u_1^0}{\partial t} = -g\frac{\partial \eta^0}{\partial x} + A_v \frac{\partial^2 u_1^0}{\partial z^2} \tag{A.2}$$

The leading order momentum equation for the bottom layer:

$$\frac{\partial u_2^0}{\partial t} = -g\frac{\partial \zeta^0}{\partial x} - g\frac{\rho_1}{\rho_2}\left(\frac{\partial \eta^0}{\partial x} - \frac{\partial \zeta^0}{\partial x}\right) + A_v \frac{\partial^2 u_2^0}{\partial z^2} \tag{A.3}$$

Solutions are written using complex amplitudes:

$$u^0 = \Re(Ue^{i\sigma t}) \qquad w^0 = \Re(We^{i\sigma t}) \qquad \eta^0 = \Re(Ee^{i\sigma t}) \qquad \zeta^0 = \Re(Ze^{i\sigma t})$$

Substituting these expressions into Eq. A.2 and Eq. A.3 yields the following differential equations

$$i\sigma U_1 = -g\frac{dE}{dx} + A_v \frac{\partial^2 U_1}{\partial z^2} \qquad i\sigma U_2 = -g\left(1-\frac{\rho_1}{\rho_2}\right)\frac{dZ}{dx} - g\frac{\rho_1}{\rho_2}\frac{dE}{dx} + A_v\frac{\partial^2 U_2}{\partial z^2}$$

These differential equations can be solved in the vertical direction, calculating a homogeneous and particular solution. This yields

$$U_1 = c_1 e^{rz} + c_2 e^{-rz} - \frac{g}{i\sigma}\frac{dE}{dx} \qquad U_2 = c_3 e^{rz} + c_4 e^{-rz} - \frac{g}{i\sigma}\left(1-\frac{\rho_1}{\rho_2}\right)\frac{dZ}{dx} - \frac{g}{i\sigma}\frac{\rho_1}{\rho_2}\frac{dE}{dx} \tag{A.4}$$

Where $r = \sqrt{\frac{i\sigma}{A_v}}$. Integration constants c_1, c_2, c_3 and c_4 appear after integration over z and may thus be functions of x.
The the no-stress boundary condition at the free surface (Eq. 2.35) is used to find $c_1 = c_2$. Then the continuity boundary conditions at the interface (Eq. 2.39 and Eq. 2.40) and the partial slip boundary condition at the bottom (Eq. 2.37) are used to find c_1, c_3 and c_4. This yields the following equations:

$$\begin{aligned}
c_1 e^{-rh} + c_1 e^{rh} - c_3 e^{-rh} - c_4 e^{rh} &= -\frac{g}{i\sigma}\left(1-\frac{\rho_1}{\rho_2}\right)\frac{dZ}{dx} + \frac{g}{i\sigma}\left(1-\frac{\rho_1}{\rho_2}\right)\frac{dE}{dx} \\
c_1 e^{-rh} - c_1 e^{rh} - c_3 e^{-rh} + c_4 e^{rh} &= 0 \\
c_3(A_v r - s_f)e^{-rH} - c_4(A_v r - s_f)e^{rH} &= -s_f\frac{g}{i\sigma}\left(1-\frac{\rho_1}{\rho_2}\right)\frac{dZ}{dx} - s_f\frac{g}{i\sigma}\frac{\rho_1}{\rho_2}\frac{dE}{dx}
\end{aligned}$$

This system of equations is written as a matrix equation:

$$A\begin{bmatrix} c_1 \\ c_3 \\ c_4 \end{bmatrix} = f$$

$$A = \begin{bmatrix} e^{-rh}+e^{rh} & -e^{-rh} & -e^{rh} \\ e^{-rh}-e^{rh} & -e^{-rh} & e^{rh} \\ 0 & (A_v r - s_f)e^{-rH} & -(A_v r - s_f)e^{rH} \end{bmatrix} \qquad f = \begin{bmatrix} -\frac{g}{i\sigma}\left(1-\frac{\rho_1}{\rho_2}\right)\frac{dZ}{dx} + \frac{g}{i\sigma}\left(1-\frac{\rho_1}{\rho_2}\right)\frac{dE}{dx} \\ 0 \\ -s_f\frac{g}{i\sigma}\left(1-\frac{\rho_1}{\rho_2}\right)\frac{dZ}{dx} - s_f\frac{g}{i\sigma}\frac{\rho_1}{\rho_2}\frac{dE}{dx} \end{bmatrix}$$

The inverse of matrix A is found using Gauss-Jordan elimination. This yields the following expressions for c_1, c_3 and c_4.

$$\begin{aligned}
c_1 = {} & \left(\tfrac{1}{2}e^{-rh} + \frac{1}{\alpha}(A_v r - s_f)e^{-rH}\sinh(rh)\right)\left(-\frac{g}{i\sigma}\left(1-\frac{\rho_1}{\rho_2}\right)\frac{dZ}{dx} + \frac{g}{i\sigma}\left(1-\frac{\rho_1}{\rho_2}\right)\frac{dE}{dx}\right) \\
& + \frac{1}{\alpha}\left(-s_f\frac{g}{i\sigma}\left(1-\frac{\rho_1}{\rho_2}\right)\frac{dZ}{dx} - s_f\frac{g}{i\sigma}\frac{\rho_1}{\rho_2}\frac{dE}{dx}\right) \\
c_3 = {} & \sinh(rh)\left(\frac{1}{\alpha}(A_v r - s_f) - 1\right)\left(-\frac{g}{i\sigma}\left(1-\frac{\rho_1}{\rho_2}\right)\frac{dZ}{dx} + \frac{g}{i\sigma}\left(1-\frac{\rho_1}{\rho_2}\right)\frac{dE}{dx}\right) \\
& + \frac{1}{\alpha}\left(-s_f\frac{g}{i\sigma}\left(1-\frac{\rho_1}{\rho_2}\right)\frac{dZ}{dx} - s_f\frac{g}{i\sigma}\frac{\rho_1}{\rho_2}\frac{dE}{dx}\right) \\
c_4 = {} & \frac{1}{\alpha}(A_v r - s_f)e^{-rH}\sinh(rh)\left(-\frac{g}{i\sigma}\left(1-\frac{\rho_1}{\rho_2}\right)\frac{dZ}{dx} + \frac{g}{i\sigma}\left(1-\frac{\rho_1}{\rho_2}\right)\frac{dE}{dx}\right) \\
& + \frac{1}{\alpha}\left(-s_f\frac{g}{i\sigma}\left(1-\frac{\rho_1}{\rho_2}\right)\frac{dZ}{dx} - s_f\frac{g}{i\sigma}\frac{\rho_1}{\rho_2}\frac{dE}{dx}\right)
\end{aligned}$$

Where the coefficient $\alpha = -2\left(A_v r\sinh(rH) + s_f\cosh(rH)\right)$ is introduced for brevity.
The expressions for U_1 and U_2 (Eq. A.4) are now substituted in the depth-averaged continuity equations (Eq. 2.42 and Eq. 2.43). This yields a coupled system of ordinary differential equations for E and Z:

$$\begin{aligned}
T_1\frac{d^2Z}{dx^2} + T_2\frac{d^2E}{dx^2} + T_3\frac{dZ}{dz} + T_4\frac{dE}{dx} - i\sigma Z + i\sigma E = 0 \\
R_1\frac{d^2Z}{dx^2} + R_2\frac{d^2E}{dx^2} + R_3\frac{dZ}{dz} + R_4\frac{dE}{dx} + i\sigma Z = 0
\end{aligned}$$

$$\begin{aligned}
T_1 = {} & \left(\left(\tfrac{1}{2}e^{-rh} + \frac{1}{\alpha}(A_v r - s_f)e^{-rH}\sinh(rh)\right)\cdot\frac{-g}{i\sigma}\left(1-\frac{\rho_1}{\rho_2}\right) + \frac{1}{\alpha}\cdot -s_f\frac{g}{i\sigma}\left(1-\frac{\rho_1}{\rho_2}\right)\right)\frac{2}{r}\sinh(rh) \\
T_2 = {} & \left(\left(\tfrac{1}{2}e^{-rh} + \frac{1}{\alpha}(A_v r - s_f)e^{-rH}\sinh(rh)\right)\cdot\frac{g}{i\sigma}\left(1-\frac{\rho_1}{\rho_2}\right) + \frac{1}{\alpha}\cdot -s_f\frac{g}{i\sigma}\frac{\rho_1}{\rho_2}\right)\frac{2}{r}\sinh(rh) - \frac{g}{i\sigma}h \\
T_3 = {} & \frac{2}{r}\sinh^2(rh)(A_v r - s_f)\left(\frac{-r}{\alpha}e^{-rH}\frac{dH}{dx} + \frac{r}{2}e^{-rH}\frac{dH}{dx}\frac{A_v r\cosh(rH) + s_f\sinh(rH)}{(A_v r\sinh(rH) + s_f\cosh(rH))^2}\right)\cdot\frac{-g}{i\sigma}\left(1-\frac{\rho_1}{\rho_2}\right) \\
& + \frac{2}{r}\sinh(rh)\cdot\tfrac{1}{2}r\frac{dH}{dx}\frac{A_v r\cosh(rH) + s_f\sinh(rH)}{(A_v r\sinh(rH) + s_f\cosh(rH))^2}\cdot -s_f\frac{g}{i\sigma}\left(1-\frac{\rho_1}{\rho_2}\right) \\
T_4 = {} & \frac{2}{r}\sinh^2(rh)(A_v r - s_f)\left(\frac{-r}{\alpha}e^{-rH}\frac{dH}{dx} + \frac{r}{2}e^{-rH}\frac{dH}{dx}\frac{A_v r\cosh(rH) + s_f\sinh(rH)}{(A_v r\sinh(rH) + s_f\cosh(rH))^2}\right)\cdot\frac{g}{i\sigma}\left(1-\frac{\rho_1}{\rho_2}\right) \\
& + \frac{2}{r}\sinh(rh)\cdot\tfrac{1}{2}r\frac{dH}{dx}\frac{A_v r\cosh(rH) + s_f\sinh(rH)}{(A_v r\sinh(rH) + s_f\cosh(rH))^2}\cdot -s_f\frac{g}{i\sigma}\frac{\rho_1}{\rho_2}
\end{aligned}$$

$$
\begin{aligned}
R_1 = &\left(\frac{e^{-rh}}{r} - \frac{e^{-rH}}{r}\right)\left(\sinh(rh)\left(\frac{1}{\alpha}(A_v r - s_f)e^{-rH} - 1\right)\cdot\frac{-g}{i\sigma}\left(1-\frac{\rho_1}{\rho_2}\right) + \frac{1}{\alpha}\cdot -s_f\frac{g}{i\sigma}\left(1-\frac{\rho_1}{\rho_2}\right)\right)\\
&-\left(\frac{e^{rh}}{r} - \frac{e^{rH}}{r}\right)\left(\frac{1}{\alpha}(A_v r - s_f)e^{-rH}\sinh(rh)\cdot\frac{-g}{i\sigma}\left(1-\frac{\rho_1}{\rho_2}\right) + \frac{1}{\alpha}\cdot -s_f\frac{g}{i\sigma}\left(1-\frac{\rho_1}{\rho_2}\right)\right)\\
&+\frac{g}{i\sigma}\left(1-\frac{\rho_1}{\rho_2}\right)h - \frac{g}{i\sigma}\left(1-\frac{\rho_1}{\rho_2}\right)H\\
R_2 = &\left(\frac{e^{-rh}}{r} - \frac{e^{-rH}}{r}\right)\left(\sinh(rh)\left(\frac{1}{\alpha}(A_v r - s_f)e^{-rH} - 1\right)\cdot\frac{g}{i\sigma}\left(1-\frac{\rho_1}{\rho_2}\right) + \frac{1}{\alpha}\cdot -s_f\frac{g}{i\sigma}\frac{\rho_1}{\rho_2}\right)\\
&-\left(\frac{e^{rh}}{r} - \frac{e^{rH}}{r}\right)\left(\frac{1}{\alpha}(A_v r - s_f)e^{-rH}\sinh(rh)\cdot\frac{g}{i\sigma}\left(1-\frac{\rho_1}{\rho_2}\right) + \frac{1}{\alpha}\cdot -s_f\frac{g}{i\sigma}\frac{\rho_1}{\rho_2}\right)\\
&+\frac{g}{i\sigma}\frac{\rho_1}{\rho_2}h - \frac{g}{i\sigma}\frac{\rho_1}{\rho_2}H\\
R_3 = &\left(\frac{e^{-rh}}{r} - \frac{e^{-rH}}{r}\right)\sinh(rh)(A_v r - s_f)\left(\frac{1}{\alpha}\cdot -re^{-rH}\frac{dH}{dx} + e^{-rH}\frac{r}{2}\frac{dH}{dx}\frac{A_v r\cosh(rH) + s_f\sinh(rH)}{(A_v r\sinh(rH) + s_f\cosh(rH))^2}\right)\\
&\cdot\frac{-g}{i\sigma}\left(1-\frac{\rho_1}{\rho_2}\right) + \left(\frac{e^{-rh}}{r} - \frac{e^{-rH}}{r}\right)\frac{r}{2}\frac{dH}{dx}\frac{A_v r\cosh(rH) + s_f\sinh(rH)}{(A_v r\sinh(rH) + s_f\cosh(rH))^2}\cdot -s_f\frac{g}{i\sigma}\left(1-\frac{\rho_1}{\rho_2}\right)\\
&-\left(\frac{e^{rh}}{r} - \frac{e^{rH}}{r}\right)\sinh(rh)(A_v r - s_f)\left(\frac{1}{\alpha}\cdot -re^{-rH}\frac{dH}{dx} + e^{-rH}\frac{r}{2}\frac{dH}{dx}\frac{A_v r\cosh(rH) + s_f\sinh(rH)}{(A_v r\sinh(rH) + s_f\cosh(rH))^2}\right)\\
&\cdot\frac{-g}{i\sigma}\left(1-\frac{\rho_1}{\rho_2}\right) - \left(\frac{e^{rh}}{r} - \frac{e^{rH}}{r}\right)\frac{r}{2}\frac{dH}{dx}\frac{A_v r\cosh(rH) + s_f\sinh(rH)}{(A_v r\sinh(rH) + s_f\cosh(rH))^2}\cdot -s_f\frac{g}{i\sigma}\left(1-\frac{\rho_1}{\rho_2}\right)\\
&\frac{-g}{i\sigma}\left(1-\frac{\rho_1}{\rho_2}\right)\frac{dH}{dx} + e^{-rH}\frac{dH}{dx}\sinh(rh)\left(\frac{1}{\alpha}(A_v r - s_f) - 1\right)\cdot\frac{-g}{i\sigma}\left(1-\frac{\rho_1}{\rho_2}\right)\\
&+e^{-rH}\frac{dH}{dx}\frac{1}{\alpha}\cdot -s_f\frac{g}{i\sigma}\left(1-\frac{\rho_1}{\rho_2}\right) + \frac{dH}{dx}\frac{1}{\alpha}(A_v r - s_f)\sinh(rh)\cdot\frac{-g}{i\sigma}\left(1-\frac{\rho_1}{\rho_2}\right)\\
&+e^{rH}\frac{dH}{dx}\frac{1}{\alpha}\cdot -s_f\frac{g}{i\sigma}\left(1-\frac{\rho_1}{\rho_2}\right)\\
R_4 = &\left(\frac{e^{-rh}}{r} - \frac{e^{-rH}}{r}\right)\sinh(rh)(A_v r - s_f)\left(\frac{1}{\alpha}\cdot -re^{-rH}\frac{dH}{dx} + e^{-rH}\frac{r}{2}\frac{dH}{dx}\frac{A_v r\cosh(rH) + s_f\sinh(rH)}{(A_v r\sinh(rH) + s_f\cosh(rH))^2}\right)\\
&\cdot\frac{g}{i\sigma}\left(1-\frac{\rho_1}{\rho_2}\right) + \left(\frac{e^{-rh}}{r} - \frac{e^{-rH}}{r}\right)\frac{r}{2}\frac{dH}{dx}\frac{A_v r\cosh(rH) + s_f\sinh(rH)}{(A_v r\sinh(rH) + s_f\cosh(rH))^2}\cdot -s_f\frac{g}{i\sigma}\frac{\rho_1}{\rho_2}\\
&-\left(\frac{e^{rh}}{r} - \frac{e^{rH}}{r}\right)\sinh(rh)(A_v r - s_f)\left(\frac{1}{\alpha}\cdot -re^{-rH}\frac{dH}{dx} + e^{-rH}\frac{r}{2}\frac{dH}{dx}\frac{A_v r\cosh(rH) + s_f\sinh(rH)}{(A_v r\sinh(rH) + s_f\cosh(rH))^2}\right)\\
&\cdot\frac{g}{i\sigma}\left(1-\frac{\rho_1}{\rho_2}\right) - \left(\frac{e^{rh}}{r} - \frac{e^{rH}}{r}\right)\frac{r}{2}\frac{dH}{dx}\frac{A_v r\cosh(rH) + s_f\sinh(rH)}{(A_v r\sinh(rH) + s_f\cosh(rH))^2}\cdot -s_f\frac{g}{i\sigma}\frac{\rho_1}{\rho_2} - \frac{g}{i\sigma}\frac{\rho_1}{\rho_2}\frac{dH}{dx}\\
&+e^{-rH}\frac{dH}{dx}\sinh(rh)\left(\frac{1}{\alpha}(A_v r - s_f) - 1\right)\cdot\frac{g}{i\sigma}\left(1-\frac{\rho_1}{\rho_2}\right)\\
&+e^{-rH}\frac{dH}{dx}\frac{1}{\alpha}\cdot -s_f\frac{g}{i\sigma}\frac{\rho_1}{\rho_2} + \frac{dH}{dx}\frac{1}{\alpha}(A_v r - s_f)\sinh(rh)\cdot\frac{g}{i\sigma}\left(1-\frac{\rho_1}{\rho_2}\right)\\
&+e^{rH}\frac{dH}{dx}\frac{1}{\alpha}\cdot -s_f\frac{g}{i\sigma}\frac{\rho_1}{\rho_2}
\end{aligned}
$$

This system is then rewritten:

$$
\begin{aligned}
\alpha_1\frac{d^2E}{dx^2} + \alpha_2\frac{dZ}{dx} + \alpha_3\frac{dE}{dx} + \alpha_4 Z + \alpha_5 E = 0\\
\beta_1\frac{d^2Z}{dx^2} + \beta_2\frac{dZ}{dx} + \beta_3\frac{dE}{dx} + \beta_4 Z + \beta_5 E = 0
\end{aligned}
$$

$$\alpha_1 = R_1T_2 - T_1R_2 \qquad \alpha_2 = R_1T_3 - T_1R_3 \qquad \alpha_3 = R_1T_4 - T_1R_4 \qquad \alpha_4 = -i\sigma R_1 - i\sigma T_1 \qquad \alpha_5 = i\sigma R_1$$
$$\beta_1 = R_2T_1 - T_2R_1 \qquad \beta_2 = R_2T_3 - T_2R_3 \qquad \beta_3 = R_2T_4 - T_2R_4 \qquad \beta_4 = -i\sigma R_2 - i\sigma T_2 \qquad \beta_5 = i\sigma R_2$$

From the tidal forcing boundary condition for η^0 at $x = 0$ follows that $E = A$ at $x = 0$.
From the no-amplitude boundary condition for ζ^0 at $x = 0$ follows that $Z = 0$ at $x = 0$.
Boundary conditions for E and Z at $x = L$ follow from the coastal no-flow boundary condition. When $\rho_1 \neq \rho_2$ and $h \neq 0$ and $h \neq H$, this boundary condition is satisfied when $\frac{dE}{dx} = 0$ and $\frac{dZ}{dx} = 0$. When $\rho_1 = \rho_2$ or $h = 0$ or $h = H$, this boundary condition does not yield boundary conditions for E and Z and the system of differential equations cannot be solved.
To numerically solve the system, the derivatives are approximated by second-order finite difference expressions:

$$\left.\frac{d^2F}{dx^2}\right|_{x=i\cdot\Delta x} \approx \frac{F_{i+1} - 2F_i + F_{i-1}}{\Delta x^2} \qquad\qquad \left.\frac{dF}{dx}\right|_{x=i\cdot\Delta x} \approx \frac{F_{i+1} - F_{i-1}}{2\Delta X}$$

Where $F_i = F(i \cdot \Delta x)$.
The following matrix equation is set up:

$$\begin{bmatrix}
1 & 0 & 0 & 0 & 0 & 0 & \cdots & & \\
0 & 1 & 0 & 0 & 0 & 0 & \cdots & & \\
\frac{\beta_1}{\Delta x^2} - \frac{\beta_2}{2\Delta x} & \frac{-\beta_3}{2\Delta x} & \frac{-2\beta_1}{\Delta x^2} + \beta_4 & \beta_5 & \frac{\beta_1}{\Delta x^2} + \frac{\beta_2}{2\Delta x} & \frac{\beta_3}{2\Delta x} & 0 & \cdots & \\
\frac{\alpha_2}{2\Delta x} & \frac{\alpha_1}{\Delta x^2} - \frac{\alpha_3}{2\Delta x} & \alpha_4 & \frac{-2\alpha_1}{\Delta x^2} + \alpha_5 & \frac{\alpha_2}{2\Delta x} & \frac{\alpha_1}{\Delta x^2} + \frac{\alpha_3}{2\Delta x} & 0 & \cdots & \\
 & & & & \ddots & & & & \\
 & \cdots & 0 & \frac{1}{2\Delta x} & 0 & \frac{-4}{2\Delta x} & 0 & \frac{3}{2\Delta x} & 0 \\
 & \cdots & 0 & 0 & \frac{1}{2\Delta x} & 0 & \frac{-4}{2\Delta x} & 0 & \frac{3}{2\Delta x}
\end{bmatrix}
\begin{bmatrix} Z_0 \\ E_0 \\ Z_1 \\ E_1 \\ \vdots \\ Z_n \\ E_n \end{bmatrix} =
\begin{bmatrix} 0 \\ A \\ 0 \\ 0 \\ \vdots \\ 0 \\ 0 \end{bmatrix}$$

This matrix is numerically inverted to find approximations for E and Z. These are differentiated using a second-order finite difference scheme to find approximations for U_1 and U_2.

Bibliography

W.M. Cameron and D. Pritchard. *Estuaries*. John Wiley and Sons, 1963.

A. Chernetsky. *Trapings of sediment in tidal estuaries*. 2012. ISBN 978-90-5335-534-3.

Y. M. Dijkstra, R. L. Brouwer, H. M. Schuttelaars, and G. P. Schramkowski. The iflow modelling framework v2.4: a modular idealized process-based model for flow and transport in estuaries. *Geoscientific Model Development*, 10(7):2691–2713, 2017. doi: 10.5194/gmd-10-2691-2017. URL `https://www.geosci-model-dev.net/10/2691/2017/`.

Theo Gerkema. *An Introduction to Tides*. Cambridge University Press, 2019. doi: 10.1017/9781316998793.

J. Pedlosky. *Geophysical Fluid Dynamics*. (Springer-Verlag New York, 1987. ISBN 978·0·387·96387-7.

Clinton D. Winant. Two-layer tidal circulation in a frictional, rotating basin. *Journal of Physical Oceanography*, 40(6):1390–1404, 2010. doi: 10.1175/2010JPO4342.1. URL `https://doi.org/10.1175/2010JPO4342.1`.